A SINGLE-PIXEL HYPERSPECTRAL IMAGING SYSTEM FOR CANCER MARGIN DETECTION

by

Joseph Allen Peller

A dissertation submitted to the faculty of
The University of North Carolina at Charlotte
in partial fulfillment of the requirements
for the degree of Doctor of Philosophy in
Optical Science and Engineering

Charlotte

2018

Approved by:

_____
Dr. Susan Trammell

_____
Dr. Nathaniel Fried

_____
Dr. Faramarz Farahi

_____
Dr. Pinku Mukherjee

_____
Dr. Gloria Elliot

ABSTRACT

JOSEPH ALLEN PELLER. A single-pixel hyperspectral imaging system for Cancer Margin Detection.(Under the direction of DR. SUSAN TRAMMELL)

We have developed a hyperspectral imaging (HSI) system based on a single pixel camera design to detect differences in tissue properties based on the optical reflectance and autofluorescence spectra of the tissue. The long-term goal of this project is to develop an HSI system to be used as a surgical navigation aid. Surgical excision of malignant tissue continues to be the foundation of treatment for most solid mass tumors. A significant remaining challenge for cancer surgery is ensuring that no residual malignant tissue is left behind, as recurrent tumors lead to high mortality rates. Unfortunately, cancerous tissue is often indistinguishable from healthy tissue under visual inspection during surgery and there are few diagnostic imaging tools to aid the surgeon in the determination of the tumor margins in real time. Cancer surgeons are in need of additional intraoperative imaging modalities for use during surgery to clearly delineate tumor margins and identify areas of residual disease.

Recent research has demonstrated that optical spectroscopy can be used to distinguish between healthy and diseased tissue. HSI is a hybrid imaging modality that combines imaging and spectroscopy and provides a 2D image that contains spectral information in each pixel. Because HSI captures both spatial and spectral information, this technique has potential applications for noninvasive disease diagnosis and surgical guidance. Conventional HSI systems employ spatial or spectral scanning techniques that reconstruct the spectral image after scanning is complete. We are developing a different type of HSI system based on a single pixel camera design. The single pixel design provides

an imaging architecture that is more flexible than traditional HSI scanning techniques and can provide better performance in several key areas including improved operation at low light levels and enhanced dynamic range.

A single pixel camera uses a single detector to create a 2-D image of a scene rather than using an array of detectors. The design of a single-pixel camera relies on the mathematical theory and algorithms of compressive sampling (CS), which is based on the idea that a small number of linear projections of a compressible image contain enough information for reconstruction. A single-pixel camera uses a digital micromirror device (DMD) as a spatial light modulator to optically calculate linear projections of a scene onto pseudo-random binary patterns. Hadamard matrices are used as the binary patterns. A single-pixel imaging system produces an image by rapidly obtaining many measurements of the intensity of a scene using different Hadamard matrices. The signal and the corresponding Hadamard code are saved for reconstruction, which occurred after all codes had been displayed on the DMD. This method of single-pixel imaging based on CS can be made hyperspectral by replacing the single detector with a spectrometer.

The HSI system was built and images of known objects were acquired to test the spectral and spatial resolution of the camera and to determine operating parameters for future studies. The software necessary to acquire and reconstruct images was developed in LabView and Matlab. The test images were imaged in fluorescence and reflectance modes simulating future study conditions. The compressive error was tested and relations between image reconstruction quality and the number of Hadamard codes sent to the DMD were quantified.

The ability of the single-pixel HSI system to distinguish between healthy and unhealthy tissue was initially tested using an *ex vivo* porcine tissue model. The autofluorescence emission from collagen (400 nm) and NAD(P)H (475 nm) along with differences in the optical reflectance spectra were used to differentiate between healthy and thermally damaged tissue. Thermal lesions were created in porcine skin (n = 12) and liver (n=15) samples using an IR laser. The damaged regions were clearly visible in the hyperspectral images. Sizes of the thermally damaged regions as measured via hyperspectral imaging were compared to sizes of these regions as measured in white light images and via physical measurement. Good agreement between the sizes measured in the hyperspectral images, white light imaging and physical measurements was found. The HSI system can differentiate between healthy and damaged tissue.

The ability of the HSI system to distinguish between healthy and cancerous tissue was evaluated by imaging human pancreatic tissue samples *ex vivo*. Differences in the optical reflectance spectra were used to identify healthy and malignant pancreatic tissue. Tissue samples from 20 patients were imaged with the HSI system and these images were compared to white light and histological analysis of these samples. An overall sensitivity of 74.80±9.18% and a specificity of 68.59±10.43% as measured from reflectance HSI was found which confirms the system is sensitive to the changes in tissue caused by the presence pancreatic cancer. Differences in the optical autofluorescence emission from collagen (400 nm) and NAD(P)H (475 nm) were also used to identify healthy and malignant pancreatic tissue in a small subset of samples (n=2).

Finally, polarization imaging capability was added to the HSI system. Thermal lesions were created in porcine skin (n = 8) samples using an IR laser. Sizes of the

thermally damaged regions as measured via hyperspectral polarization imaging were compared to sizes of these regions as measured in reflectance HSI and white light imaging of the samples. Good agreement between the sizes measured in the polarization HSI, reflectance HSI and white light images was found. These results confirmed the sensitivity of the camera to changes in the tissues polarization properties.

DEDICATION

This dissertation is dedicated to several people.

Firstly, to my family. To my mom and dad and brothers, who have encouraged me from a young age to always keep learning, trying, and doing what makes me happy. Who have supported me and given advice and comfort whenever I needed it during this long process.

To my friends, to those who I met during the long half decade we spent together in grad school, for the not just the academic help but for the sense of kinship and community we built up to support each other over the years. We are all about to go our separate ways and I know that I personally am bad at keeping up wish, but I wish everyone of you the best of luck in the future. Chris, Madison, Charlotte, Abby, Francis, Zeba, Geoff. Thank you.

And finally to Alex, I have no words for how much your patience and love has meant to me over this process. The many times I've come home fuming and frustrated over some small hang up only to have you help calm me down and consider things rationally. From little things like making sure I'm prepared for a conference, to surprise weekends away so we could both clear our heads from the week, to putting your own art career on hold for a few years so I could finish this. You are going to do great things, and I'm looking forward to spending our lives together.

I couldn't have done this on my own, thank you all.

ACKNOWLEDGEMENTS

I would like to begin by thanking the Levine Cancer Institute for funding these studies. Including a special thank you to the HPB group at CMC for the assistance in the pancreatic tissue experiment and all the Pas in the pathology lab who put us up in their workspace for over a year.

Thank you to Charlotte Teacher Institute for the assistance over the summers and the chance to share not just this research but the research process to a fantastic and engaged group of teachers.

Thanks to all the undergrads who have assisted in this project over the years. Aubrey, Andrew, Amanda, Nancy, your diligence in data collection made this whole process run so much smoother then it could have.

Finally, I would also like to thank Dr. Fried for supplying the IR lasers used in chapters 3 and 5 of this dissertation.

TABLE OF CONTENTS

LIST OF TABLES

LIST OF FIGURES

1. Introduction

1.1 Motivation

In 2017, an estimated 15.5 million American's were either cancer patients or survivors and that number is expected to rise over the next decade. The most prevalent types of cancers are those that form hard collagen rich tumors, known as solid mass tumors. [1] The most common treatment of solid mass tumors is surgical excision in conjunction with chemotherapy and/or radiation therapy. The goal of the surgical excision is to remove all diseased tissue, but this is often balanced by a need to preserve healthy tissue. For example, the standard course of treatment for many breast cancer patients is tissue-conserving lumpectomy and for pancreatic cancer, sparing healthy tissue is important to preserve digestive function and the ability to produce insulin.

Multiple imaging modalities are available for preoperative tumor diagnosis and surgical planning, including x-ray, ultrasound, computed tomography (CT), magnetic resonance imaging (MRI), positron emission tomography (PET) and single photon emission computed tomography (SPECT). However, these techniques are not usually available during surgery. Paraffin section of inked surgical margins is the gold standard for margin assessment. Unfortunately, this process is time consuming and results are not available until several days after surgery. Typically, surgeons determine the tumor resection margins during procedures based on palpation, visual inspection and frozen section histology. In some cases, intraoperative ultrasound is used to guide tissue excision. [2] A danger to the patient exists if any residual cancerous cells are not removed in the resection. Missing these cells leads to a higher rate of local reoccurrence of cancer in the tissue even when followed up by chemotherapy and radiation. [3] Consequently, the

success of cancer surgery depends on a doctor's ability to visualize the margins of the tumor to be removed. There is not yet a standard method to determine these margins intraoperatively. Cancer surgeons need additional intraoperative imaging modalities for use during surgery to clearly delineate tumor margins and identify areas of residual disease.

We are developing a hyperspectral imaging system (HSI) to detect gross tumor margins using fluorescent and reflectance imaging in real-time. The long term goal of this project is to eliminate the need for frozen section histology, reduce the amount of time needed to complete the surgical procedure, increase the accuracy of tissue resection, and improve patient outcomes.

1.2 Fluorescence Spectroscopy and Cancer Detection

Fluorescence occurs when photons impart energy to bound electrons in atoms and molecules. For most materials, the excited electron will quickly release this extra energy when the excited electron drops to a lower energy state and the atom or molecule emits a photon. If the emitted photon has the same frequency as the excitation photon, this process is called resonance fluorescence. In complex molecules energy can be released through vibrational relaxation while the electron is in the excited state and then this is followed by radiative decay. In this case, the emitted photon will have a lower energy than the one that originally excited the molecule. [4] This process of excitation followed by fluorescence takes place on short time scales (200 ns – few μs). [5] A simplified example is shown in Figure 1. An initial photon raises the energy of an electron to the S2 state. The electron then loses energy through non-radiative processes to the S1 state.

Finally, it returns to the ground state releasing a photon of a longer wavelength than the one that initially excited the atom. [4]

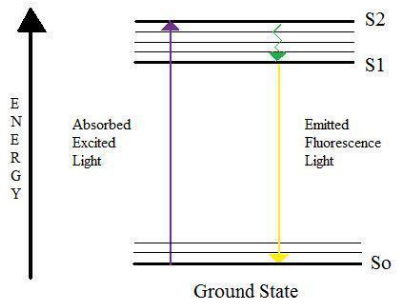

Figure 1. This figure shows an example of fluorescence in a simplified three level model of an atom.

Fluorescence can be used to identify specific molecules and is becoming an important tool for cancer diagnosis. Fluorescent dyes that bind to specific proteins have been used in biology for more than 20 years. A dye is injected into the tissue where it is absorbed by cells. When the tissue is illuminated by a specific light source the dye fluoresces. These fluorescent dyes can be used to target specific organelles and proteins [6] and multiple dyes can be used to simultaneously highlight specific features in tissues or cellular structures. The disadvantage of this technique is that it is sensitive to cellular metabolism, and insuring uniform uptake over a large area of tissue is difficult.

Autofluorescence is fluorescent emission under UV illumination by proteins that naturally exist in tissue. Since the early nineties the autofluorescence of tissue proteins has been recognized as a marker of changes in the makeup and structure of tissue and a potential tool for cancer detection. Initially this spectroscopic technique was used to observe differences in the spectra of healthy and abnormal cells on a microscopic level. The autofluorescence of collagen near 400 nm and nicotinamide adenine dinucleotide

phosphate, NAD(P)H, near 475 nm were noted for their high sensitivity to the presence of a range of different cancers in these early experiments. [7-9]

Recent research has shown that autofluorescent spectroscopy can be used to distinguish between healthy and diseased tissue and may become an important minimally invasive diagnostic tool for a range of diseases including breast cancer [10], colon cancer [11], cervical cancer [12], and Barrett's esophagus. [13] Autofluorescence radiation is emitted by the natural constituents of tissue when the tissue is illuminated by a laser source. No exogenous fluorescent substances are added to the tissue. Consequently, laser-induced autofluorescence spectra give accurate information about the content and molecular structure of the emitting tissue and may signal small modifications of any of them. For example, Chandra et al. illuminated excised pancreatic tissue with 355 nm laser radiation to excite autofluorescent emission from collagen and NAD(P)H [14] By measuring the ratio of the resulting emission peaks it is possible to distinguish healthy and diseased tissue in gross tissue samples. [14] Figure 2 shows the change in the autofluorescence spectrum for healthy and cancerous pancreatic tissue. The two peaks correspond to collagen and NADH at 400 nm and 475 nm respectively. Note that the carcinoma has a much higher collagen peak than healthy tissue. This indicates an increase in fibrosis in the tissue. The steep rise in the peak around 400 nm corresponding to an increase in collagen fluorescence. [15] By comparing this change in the collagen signal to the relatively stable NADPH fluorescence peak, the autofluorescence can be used as a biomarker for cancer.

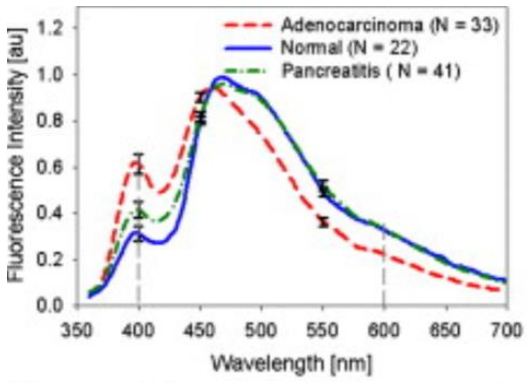

Figure 2: This graph shows mean fluorescence spectra obtained from human pancreatic tissue containing normal tissue (blue solid line), inflamed tissue (pancreatitis; green dot-dash line), and adenocarcinoma (red dashed line). [15]

1.3 Reflectance Spectroscopy and Cancer Imaging

Another method of optical histology is the examination of the reflectance spectrum of bulk tissue. To obtain a reflectance spectrum, tissue is illuminated with a continuous light source and the spectrum of the reflected light is collected. Reflectance spectroscopy provides information about tissue morphology, including cell size and density. Chandra et al. demonstrated that reflectance spectra of healthy and diseased pancreatic tissue differ (see Figure 3), where the largest differences are apparent near 500 nm. Reflectance spectroscopy has high specificity in detecting abnormal tissue and stronger signal strength than fluorescence. However, in general, reflectance spectroscopy has lower sensitivity than fluorescent spectroscopy due to differences in bulk tissue composition for single samples. [16-17]

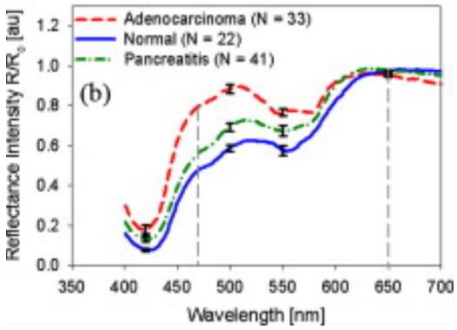

Figure 3: This graph shows mean reflectance spectra obtained from human pancreatic tissue containing normal tissue (blue solid line), inflamed tissue (pancreatitis; green dot-dash line), and adenocarcinoma (red dashed line). The two gray dotted lines indicate the wavelengths at which the greatest and least change occur in the tissue. By taking the ratio of the intensity at these two wavelengths cancer can be detected in the tissue. [16]

1.4 Combination of Reflectance and Fluorescence Spectroscopy

While both reflectance and fluorescence spectroscopy are powerful tools for cancer detection, the combination of these two techniques increases sensitivity. Several studies have shown that by correlating reflectance spectra with fluorescence spectra at the same location, the specificity and sensitivity increases up to 90%. [18]

1.5 Pancreatic Cancer

Pancreatic cancer is the third leading cause of cancer related death in the United States. Most pancreatic cancer patients die within the first year after diagnosis, and only 6% survive five years. In addition, pancreatic cancer death rates have remained constant in the past decade, in contrast to lower death rates for lung, colorectal, breast, and prostate cancers. These statistics reflect a lack of progress in prevention, early diagnosis, and treatment of the disease. [19] The research described here is developing a tool for more effective surgical treatment of pancreatic cancer.

Currently, the only curative treatment for pancreatic cancer is surgery. The most common surgery to treat pancreatic cancer is the Whipple procedure. [20] The Whipple

preserves enough of the pancreas so that the patient can produce gastric enzymes and insulin, while removing all cancerous tissue. There are two important blood vessels that supply blood to the pancreas, the super mesenteric vein (SMV) and the super mesenteric artery (SMA). If these vessels are involved with the tumor these structures must be cut and reattached. Accurately identifying tumor margins dictates how much of the pancreas to leave, and which sections of the SMA and SMV to remove. [21]

Pancreatic cancer margins are not well defined upon gross inspection because of inflammation and fibrosis associated with tumors and surrounding tissue. [22] The current method to determine resection margins is to remove small tissue samples from the suspected margins and then immediately test for the presence of cancer cells in the excised tissue via frozen section histology. The goal of this research is to provide a method for the identification of these margins in real-time.

1.6 This Project

In this study, a hyperspectral imaging (HSI) system based on a single-pixel camera design is used to examine the reflectance and autofluorescence spectra of tissue to detect malignant regions in tissue. HSI is a hybrid imaging modality that combines imaging and spectroscopy. By collecting spectral information at each position in a 2-D image, HSI generates a 3-D dataset of spatial and spectral information, known as a hypercube.

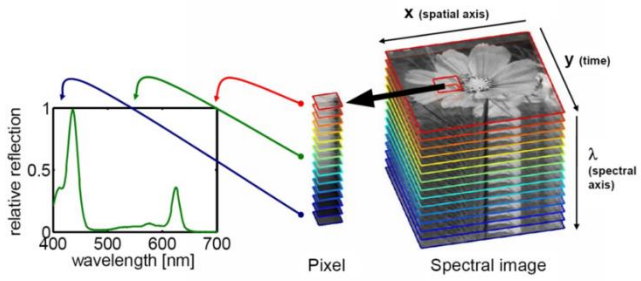

Figure 4: A hypercube of a flower. Each pixel in the image contains a continuous spectrum. [23]

Conventional HSI systems employ spatial or spectral scanning to acquire a hypercube. [24-25] Spatial scanning techniques obtain a spectrum in one location and then the object/spectrometer is translated to obtain spatial information. The full hyperspectral image is recovered after scanning is complete.

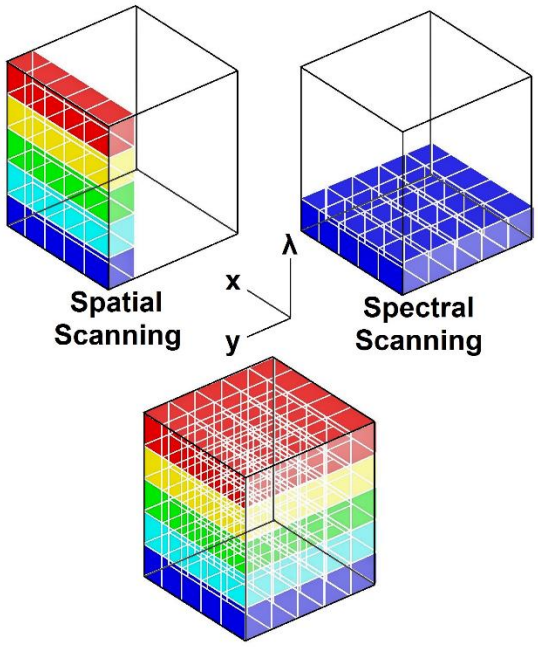

Figure 5: An example of two types of hyperspectral scanning. In spatial scanning, the entire spectrum is collected over a pixel or line scan of the image, which is then iterated over the image to create a hypercube. In spectral scanning, the entire image is collected at a specific wavelength and then the wavelength is iterated to create a hypercube. [26]

In spectral scanning a 2-D image is projected through a tunable filter or filter wheel and individual images are captured at different wavelengths. The hyperspectral image is reconstructed by combining the separate monochromatic images. Because HSI captures both spatial and spectral information, this technique has potential applications for noninvasive disease diagnosis and surgical guidance.

A single pixel camera uses a single detector to create a 2-D image of a scene rather than using an array of detectors. [27] The primary advantage of this technique over other spectral imaging systems is its potential to function at low light levels. Since in this study we aim to detect changes in protein autofluorescence and reflectance due to the presence of malignant tissue and typically these signals are weak, we chose to build a single-pixel camera as the engine of our HIS system.

This dissertation describes the design, construction and testing of this HSI system. The imaging system was constructed and its ability to capture both reflectance and fluorescence images was tested (Chapter 2). The HSI system was used to detect changes in tissue resulting from thermal damage in *ex vivo* tissue models (Chapter 3). Next, the system was used to delineate tumor boundaries in human pancreatic tissue samples *ex vivo* and compared to histology. (Chapter 4) Finally, polarization imaging capability was added to the system and this was tested on *ex vivo* tissue models (Chapter 5).

2. Design and Testing of a Single-Pixel Hyperspectral Imaging System for the Detection of Fluorescent and Reflectance Spectra

2.1 Single-Pixel Hyperspectral Imaging

In this chapter the design and testing of a single-pixel hyperspectral imaging (HSI) system is discussed. Hyperspectral imaging is a technique that provides

both spatial and spectral information of a scene as discussed in Chapter 1. Traditional imaging systems use a pixel array to capture information, where each pixel in the image contains information about the intensity of the light measured as a function of position. In a hyperspectral image, an extra dimension of data is added in that each pixel also contains the spectral information. HSI differs from colorized or multispectral imaging in terms off spectral resolution. HSI has spectral resolution on the nanometer scale, while multispectral imaging uses wider spectral bands. Because HSI captures both spatial and spectral information, this technique has potential applications for noninvasive disease diagnosis and surgical guidance. HSI has been applied to a range of diseases including colon, breast, and cervical cancers[10-12]

A single pixel camera uses a single detector to create a 2-D image of a scene rather than using an array of detectors. [27] The design of a single-pixel camera relies on the mathematical theory and algorithms of compressive sampling (CS), which is based on the idea that a small number of linear projections of a compressible image contain enough information for reconstruction. A single-pixel camera based on CS combines sampling and compression into a single measurement in that the camera directly acquires a condensed representation of the data set. The traditional approach to digital data acquisition samples a signal uniformly at or above the Nyquist rate. Using a conventional digital camera as an example, the samples are obtained by a 2-D array of N pixels. N is very large in digital cameras (megapixel arrays) and the raw data is often compressed in data formats such as JPEG, for storage after acquisition. Compression algorithms are used to store a fraction of the measurements, but retain the ability to recover the full 2-D image. CS bypasses the sampling process, and directly acquires a condensed

representation of the data set. A single-pixel camera based on CS acquires a series of intensity measurements from a scene and then the full 2-D image is reconstructed based on this sampling.

A single-pixel camera uses a digital micromirror device (DMD) as a spatial light modulator to optically calculate linear projections of a scene onto pseudo-random binary patterns. A DMD is a reflective spatial light modulator that selectively redirects parts of a light beam (see Figure 6). The DMD is made up of small, electrostatically actuated micromirrors.

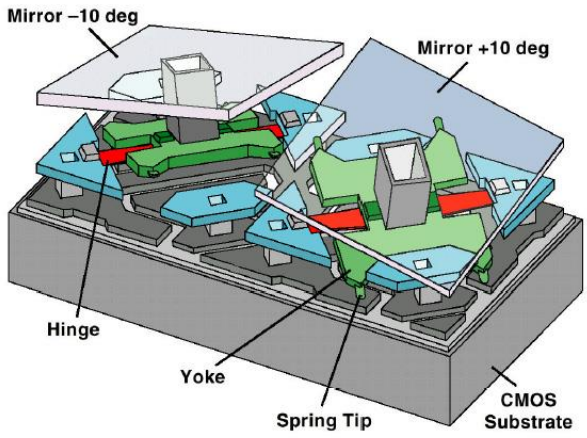

Figure 6: An example of the mirrors on a digital micromirror device. Each mirror can be moved to different states corresponding to different angles of tilt, which allows them to direct light and act as a spatial light modulator. [28]

Hadamard matrices, which fulfill the sparsity requirements for CS, are used as the binary patterns. A single-pixel imaging system produces an image by rapidly obtaining many measurements of the intensity of a scene using different Hadamard matrices. The signal and the corresponding Hadamard code are saved for reconstruction, which occurred after all codes had been displayed on the DMD. This method of single-pixel

imaging based on CS can be made hyperspectral by replacing the single detector with a spectrometer. The dispersive element of the spectrometer spreads the light across the linear detector array and each pixel along the array corresponds to a single pixel detector operating at a specific wavelength. The reconstruction of the image can be performed using any of the pixels, which corresponds to a reconstruction as a function of wavelength, or HSI. [29]

CS theory offers a sensing framework that makes it possible to reconstruct signals from very few measurements and has found many applications in optics. Other researchers have developed compressive spectral imaging systems based on the single-pixel-camera design [30-31], coded apertures [32-34], and schemes based on spectral modulation. [35]

The long-term goal of this project is to construct a HSI system based on a single-pixel design that can differentiate between healthy and diseased tissue at a video rate for use as a surgical guidance tool. This is a new application of single pixel HSI. The primary advantage of a single-pixel HSI system design over other HSI systems is the potential of a single-pixel system to function even when light levels are very low and therefore the signal to noise ratio is poor. Since in this study we aim to detect changes in protein autofluorescence and reflectance and typically these signals are very weak, we have chosen to build a single-pixel camera as the engine of our HSI system.

2.3 Methods

2.3.1 Single-Pixel Camera Design and Construction

A schematic of the HSI system is shown in Figure 7. The imaging system was mounted on a vertical stage and imaged an area on an imaging stage (see Figure 7). A halogen lamp (150 W, Model I-150 Optical Fiber Light Source, Cuda) was used as the source for to illuminate test objects and was mounted 23° from the vertical axis and aligned to illuminate the stage. A DLP5500 0.55″ XGA with 1024 x 768 pixels DMD was used in the system. The signal was collected through focusing optics into an Ocean Optics HR4000 Spectrometer with a 200 μm slit and 600 line/mm grating, resulting in a spectral range of 355-800 nm and a dispersion of 0.12 nm/pix. To collect an image, a series of 32 x 32 pixel wide Hadamard matrices was programmed onto the DMD and a signal was collected for each code. The signal and the corresponding Hadamard code were saved for reconstruction, which occurred after all codes had been displayed. The spatial resolution of the system is set by a combination of the size of the pixels used in the binary codes used on the DMD and the focusing optics of the camera providing a spatial resolution of 0.5 mm/pixel, and a FOV of 1.4 cm x 1.4 cm. LabVIEW software was used to manipulate the DMD and capture the signal from the spectrometer. After image acquisition a MATLAB program based on the NESTA algorithm [36] was used to reconstruct the images.

The camera design was updated after initial testing to be more sensitive to the fluorescence signal and to improve the spatial resolution. The same DMD and setup (see Figure 7) were used in the updated system. The sensitivity of the imaging system was improved by replacing the original spectrometer with an Ocean Optics QE Pro

Spectrometer. This improved the spectral range to 350-750 nm, and the dispersion to 0.335 nm/pixel. The spatial resolution of the system is set by a combination of the size of the pixels used in the binary codes used on the DMD and the focusing optics of the camera. 64 x 64 pixel Hadamard matrices were used on the DMD, and compared to 32 x 32 pixel Hadamard matrices used in the earlier system. The 32 pixel had an improved spatial resolution of 0.44 mm/pix and the 64 pixel matrices had a spatial resolution of 0.3 mm/pixel. Both imaging schemes had the same FOV of 1.9 cm x 1.9 cm.

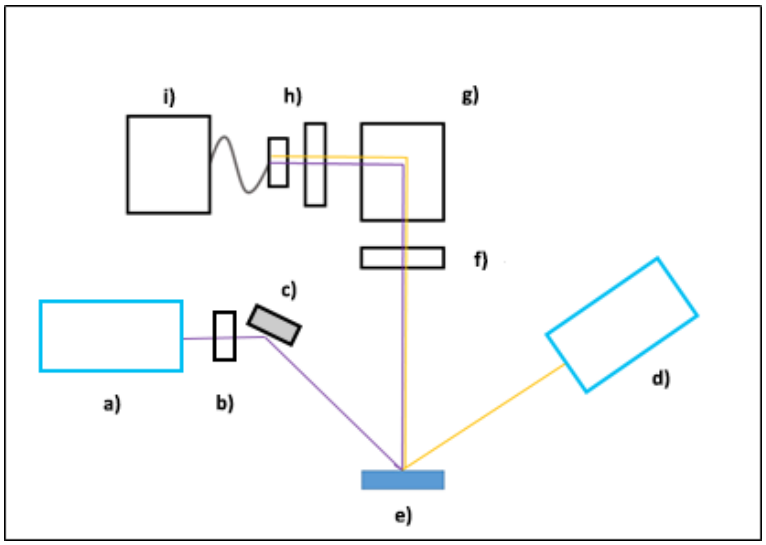

Figure 7: Schematic of the hyperspectral imaging system. The sample stage (e) is illuminated by either the nitrogen laser (a) focused through a cylindrical lens (b) and directed by a steering mirror (c) or by a halogen lamp (d). Light is collected from the sample by an imaging optic (f) and an image is formed on the DMD (g). The light is then reflected off the DMD's mirrors through a series of collection optics (h) and into a fiber where the signal is sent to a spectrometer (i).

2.3.2 Test Images

A black and white test image was used to demonstrate the imaging capabilities of the original hyperspectral system (using the HR4000 spectrometer). A broadband halogen lamp illuminated this test image and the reflected light was imaged with the HSI system (see Figure 7). In addition, the ability of the system to reconstruct an image containing

spectral information was tested. A test image was created using two highlighters. The ink from the highlighters fluoresces at two distinct peaks, 520 nm and 606 nm, when illuminated with UV light (see Figure 8). The test image was illuminated with a 405 nm LED (Thorlabs M405L2) to excite fluorescence in the highlighter image and the fluorescent signal was imaged with the hyperspectral system.

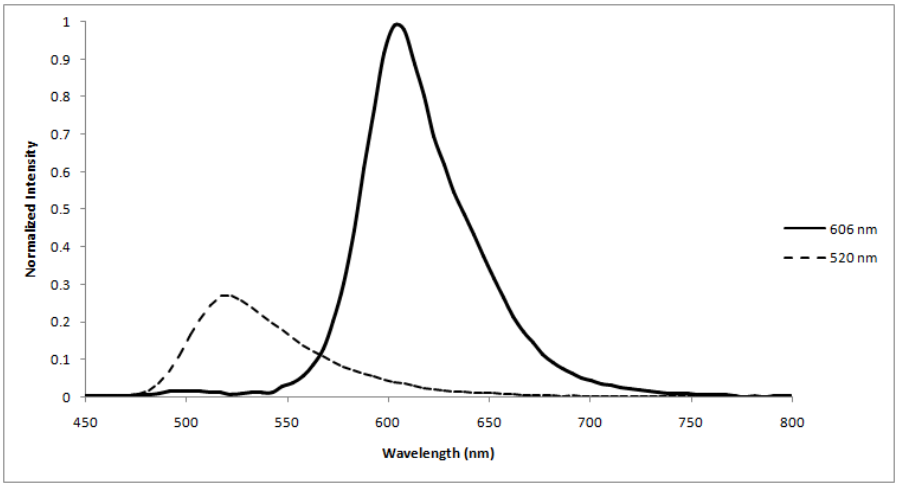

Figure 8: Fluorescent spectra of highlighter pens used to create a test image. Images were reconstructed for each fluorescent emission peak

A test image that contained spectral information was also used to evaluate the updated HSI system (the system using the QE Pro spectrometer). In this case, the reconstructed HSI was compared to an image collected by a traditional 8-megapixel CMOS array camera (iSight camera, Apple).

2.4 Results and Analysis

Figure 9 shows reconstructed images of the black and white test image obtained with the first HSI system. The image was reconstructed using 50 pixels about the peak of the halogen emission, corresponding to a 6.5 nm window centered at 650.5 nm. The effective

spatial resolution in all images is 0.5 mm per pixel and the FOV of each image is 1.4 cm x 1.4 cm. Figure 9 shows reconstructed images for three different values of M (number of Hadamard matrices used to sample the image). The maximum collection time (for 805 measurements) was approximately 15 seconds and reconstruction times were < 10 seconds. It is clear that with an increasing number of measurements, the overall quality of the reconstructed images increases. For M = 175 only a vague outline of the original picture can be discerned, while for M = 500 the major features of the image are clearly visible.

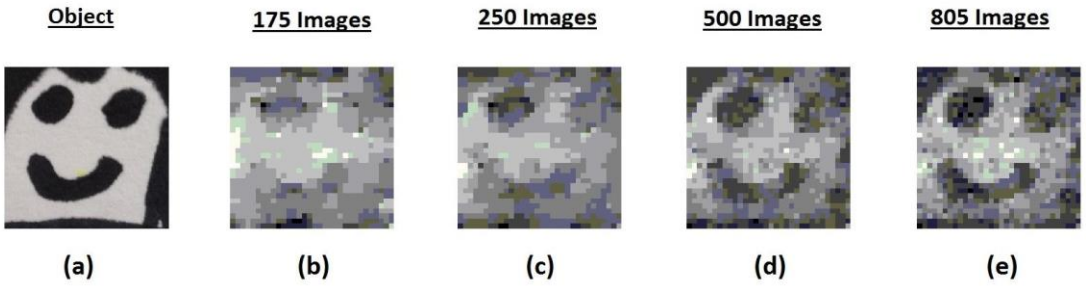

Figure 9: Reconstructed images of a black and white test image for differing numbers of measurements (M). The FOV of each image is 1.4 cm x 1.4 cm. a) The original object. b) The reconstructed image based on 175 measurements. c) The reconstructed image based on 250 measurements. d) The reconstructed image based on 500 measurements. e) The reconstructed image based on 805 measurements (the maximum number of measurements tested in this study). As M increases, the quality of the reconstructed image improves.

Figure 10 shows the results of the fluorescent test image. Two images were reconstructed corresponding to the fluorescent emission peaks of two highlighters. Both images were reconstructed using a 50-pixel window, one corresponding to a 6.5 nm window centered at 520 nm and the other to a 6.5 nm window centered at 606 nm. In addition, an image containing both fluorescent peaks were reconstructed using a 200 nm window centered at 560 nm. The effective spatial resolution in all images was 0.5 mm per pixel and the FOV of each image is 1.4 cm x 1.4 cm. The images were reconstructed from M = 804 measurements and required a total collection time < 1 minute. Figure 8 clearly

shows that the individual fluorescent peaks can be selectively imaged with the camera. Only the features that appear orange it the original image are seen in the reconstructed image that is centered on 606 nm and only the features that appear green in the original image are evident in the image centered on 520 nm. Note that the strength of the 520 nm emission peak is approximately 6 times weaker than the 606 nm peak. The reconstructed image including both fluorescent peaks shows features that appear both orange and green in the original image.

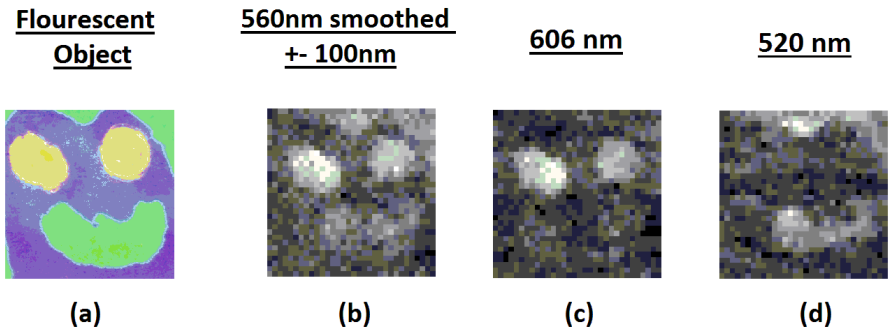

Figure 10: Original and reconstructed images of a test image based on the fluorescent signal from highlighter ink illuminated by a 405 nm LED. For all images, 805 measurements were used for the reconstruction. The FOV of each image is 1.4 cm x 1.4 cm. a) The original object. b) The reconstructed image for both fluorescent peaks. All features of the original object are evident. c) The reconstructed image centered on the 606 nm emission peak. Only the features that appear orange in the original image are evident. d) The reconstructed image centered on the 520 nm emission peak. Only the features that appear green in the original image are evident. Note that the strength of this peak is approximately 6 times weaker than the 606 nm peak.

2.4.2 Image Quality Measurements.

Figure 11 shows a full color image of a test image obtained from a traditional CMOS camera. The red channel was extracted from this image using Adobe Photoshop, and then compared to reconstructed HSI of the same test image. The HSI image was reconstructed over the wavelength range from 600 nm - 675 nm this corresponds to the red channel in a traditional RGB image. Figure 9 demonstrates that increasing the number

of sampling codes increased the image quality. As the number of Hadamard codes decreased so did the image quality of the reconstruction.

A detailed comparison of the HSI image and the red channel of the CMOS image was performed using both the average absolute error and the mean square error (MSE). Both methods are used to evaluate compression losses. The MSE is the cumulative squared error between the HSI and the red channel of the CMOS image, whereas the average absolute error measures the absolute difference between the two images. By increasing the sample numbers from 49 codes to 899 codes in the initial 32 x 32 pixel reconstruction HSI, the MSE decreases by 34.9% and the average error between the images decreased by 25.7%. For the high resolution 64x 64 pixel images were reconstructed from 3199 codes down to 899 codes. By increasing the code count from 899 to 3199, the MSE decreases by 27.3% and the average error decreases by 16.7% These trends are shown in figure 12.

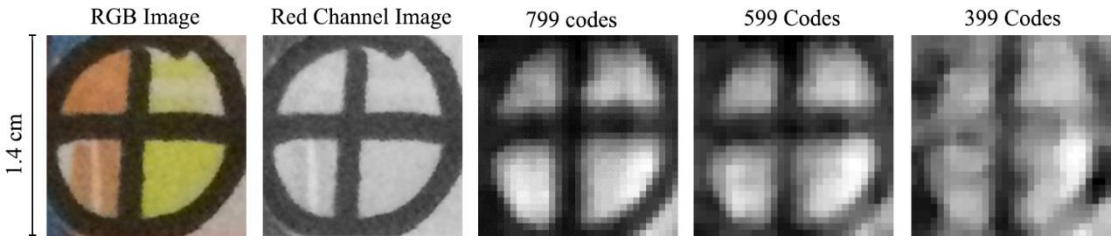

Figure 11: The original test object is shown to the left. The Red Channel image was extracted from the traditional RGB image. The other panels show 32x32 pixel HSI images based on different numbers of Hadamard codes used to reconstruct the image (799 codes, 599 codes, 399 codes).

Increasing the number of acquisition codes improves image quality. Based on these measurements, the improvement in image quality plateaus. Beyond 750 codes, in the 32 pixel images and 2700 codes in the 64 pixel images little improvement in image

quality is noted. These tests infer a limit on the minimum number of Hadamard codes that can be used to quickly and accurately reconstruct an image.

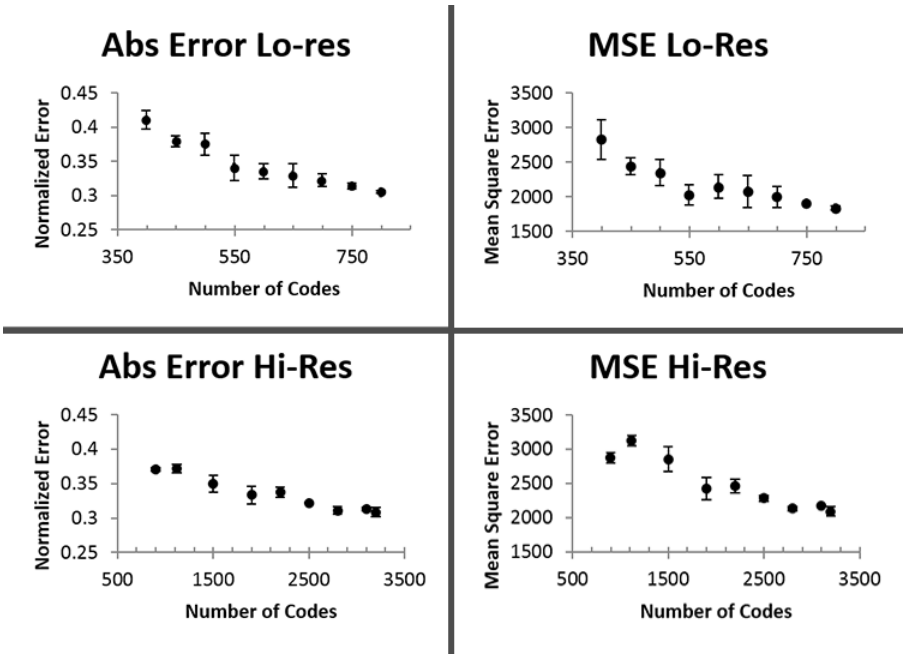

Figure 12: These plots show the effect of increasing code number in reconstruction vs image quality. In both cases the average absolute error and the MSE both decreases exponentially as code numbers are increased. This trend shows that error is inherent in the compression algorithm and a minimum error is defined by the number of codes used in reconstructing the image.

2.5 Conclusions

A HSI system based on a single-pixel camera design capable of detecting fluorescence and reflectance spectra has been constructed. Tests were conducted that showed qualitatively and quantitatively the effects of increasing code projection increased image quality in the reconstructed image. The system also showed that discrete wavelength bands of light could be selected and reconstructed with a high dynamic range. The combination of CS and high dynamic range techniques can produce images of superior dynamic range when compared to traditional imaging techniques. [41] Although not presented in this chapter, single-pixel HSI also allows the user to adjust the size of

pixels on the DMD. This allows the user to effectively trade FOV for spatial resolution without adjusting any optics. An example of this is presented in figure 13.

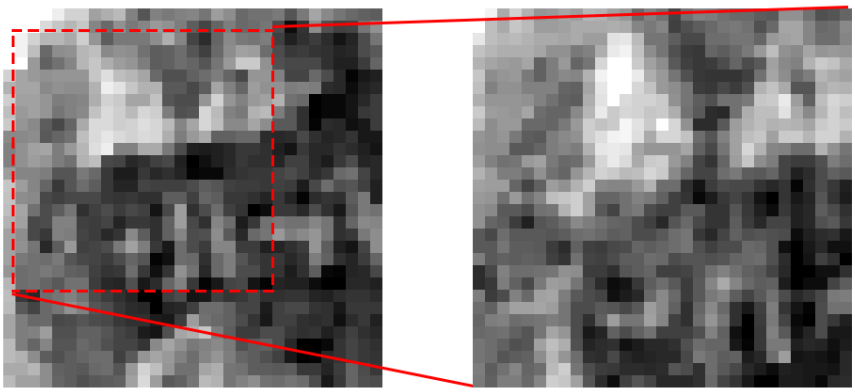

Figure 13: These reconstructions show the effect of shrinking pixel size on reconstructed HSI images. The image on the left is a reconstructed 32 x 32 image with a FOV of 1.9 cm. By decreasing the pixel size on the DMD, the camera can effectively zoom. The image on the right is a reconstructed 32 x 32 image but with a FOV of 1.1 cm. No optics were adjusted to produce the zoomed in image.

These studies show that the single-pixel HSI system can create accurate images and retrieve spectral information from the reconstructions. The next step in testing the HSI system was to assess the ability of the system to differentiate between healthy and damaged tissue.

3. Defining regions of thermal damage in ex vivo porcine tissue samples using single-pixel hyperspectral imaging

3.1 Introduction

Research has demonstrated that optical spectroscopy can be used to distinguish between healthy and diseased or damaged tissue. Both reflectance and fluorescence spectroscopy have been shown to effectively identify unhealthy tissue. [10-13]

Autofluorescence emission is produced by the natural constituents of tissue (no exogenous fluorescent substances are added) when the tissue is illuminated by UV light. The autofluorescence of collagen, near 400 nm, and nicotinamide adenine dinucleotide phosphate, NAD(P)H, near 475 nm, have been noted for their high sensitivity to the presence of a range of different diseases. [7-9] The sensitivity arises because the autofluorescence spectra of proteins change due to alterations in the makeup and structure of unhealthy tissue compared to healthy tissue. Reflectance spectroscopy provides information about tissue morphology including cell size and density. Changes in the wavelength dependence of the reflected spectrum indicate differences in the morphology and/or make up of the tissue. [24]

Hyperspectral imaging (HSI) is a hybrid imaging modality that combines imaging and spectroscopy. By collecting spectral information at each position in a 2-D image, HSI generates a 3-D dataset of spatial and spectral information, known as a hypercube. Conventional HSI systems employ spatial or spectral scanning to acquire a hypercube. [24-25] Spatial scanning techniques obtain a spectrum in one location and then the object/spectrometer is translated to obtain spatial information. The full hyperspectral image is recovered after scanning is complete. In spectral scanning a 2-D image is projected through a tunable filter or filter wheel and individual images are captured at different wavelengths. The hyperspectral image is reconstructed by combining the separate monochromatic images. Because HSI captures both spatial and spectral information, this technique has potential applications for noninvasive disease diagnosis and surgical guidance

In this study, the design and testing of a HSI system based on a single-pixel camera design is discussed. A single pixel camera uses a single detector to create a 2-D image of a scene rather than using an array of detectors. [27] The primary advantage of this technique over other spectral imaging system is its potential to function even when light level is very low and therefore the signal to noise ratio is poor. Since in this study we aim to detect changes in protein autofluorescence and reflectance due to thermal damage in porcine skin and liver ex vivo and since typically these signals are very weak we chose to build a single-pixel camera as the engine of our HIS system. The design of a single-pixel camera relies on the mathematical theory and algorithms of compressive sampling (CS). [37-39] CS is based on the idea that a small number of linear projections of a compressible image contain enough information for reconstruction. A single-pixel camera uses a digital micromirror device (DMD) as a spatial light modulator to optically calculate linear projections of a scene onto pseudo-random binary patterns. Hadamard matrices, which fulfill the sparsity requirements for CS, are used as the binary patterns. A single-pixel imaging system produces an image by rapidly obtaining many measurements of the intensity of a scene using different Hadamard matrices. This method of single-pixel imaging based on CS can be made hyperspectral by replacing the single detector with a spectrometer. The dispersive element of the spectrometer spreads the light across the linear detector array and each pixel along the array corresponds to a single pixel detector operating at a specific wavelength. The reconstruction of the image can be performed using any of the pixels, which corresponds to a reconstruction as a function of wavelength, or HSI. [29] CS theory offers a sensing framework that makes it possible to reconstruct signals from very few measurements and has found many applications in

optics. Other researchers have developed compressive spectral imaging systems based on the single-pixel-camera design [30-31], coded apertures [32-34], and schemes based on spectral modulation. [35]

The long-term goal of this project is to construct a HSI system based on a single-pixel design that can differentiate between healthy and diseased tissue at a video rate for use as a surgical guidance tool. This is a new application of single pixel HSI. A single pixel HSI system design based on CS provides improved performance compared to HSI scanning techniques for this type of application. For example, a single-pixel design offers improved sensitivity as the intensity of the compressed signal at the detector is much greater compared to the signal obtained via scanning techniques. Starling et al. successfully applied the methods from compressive sensing to create a single-pixel spectrometer capable of quickly measuring spectra with limited signal. [40] The autofluorescence signals of NAD(P)H and collagen are weak and the improved sensitivity of a single pixel design is important for accessing tissue health with HSI. In addition, most scenes in nature, including images of tissues, have more dynamic range than traditional cameras can capture. The combination of CS and high dynamic range techniques can produce images of superior dynamic range when compared to traditional imaging techniques. [41]

3.2 Methods

For this ex vivo tissue study, porcine skin and liver tissue samples of uniform thickness were cut into 2 cm x 2 cm squares. Hyperspectral reflectance imaging of both porcine skin and liver samples were obtained, while autofluorescent imaging was

obtained for skin tissue. Fluorescent imaging of the liver was not obtained due to the reabsorption of the autofluorescence by blood in the liver.

This study uses a camera with a similar design as in section 2, but has improved sensitivity and spatial resolution. The DMD in the system is a DLP5500 0.55″ XGA with 1024 x 768 pixels. The sensitivity of the imaging system was improved with the addition of a new spectrometer (Ocean Optics QE Pro Spectrometer; spectral range 350-750 nm, 1044 pixels in the linear array, and dispersion 0.335 nm/pixel). The spatial resolution of the system is set by the size of the pixels used in the binary codes used on the DMD. In this study, 64 x 64 Hadamard matrices were used on the DMD, (compared to 32 x 32 pixel codes in previous studies) with a FOV of 1.9 cm x 1.9 cm. This improved the spatial resolution from 0.44 mm/pixel to 0.30 mm/pixel. LabVIEW software is used to manipulate the DMD and capture the signal from the spectrometer.

The imaging system was mounted on a vertical stage and imaged an area on a stainless steel specimen stage (see Figure 14). A 3 mW nitrogen laser (SRS, NL100) was used as the fluorescence excitation source. The laser has a center wavelength of 337.1 nm, a 0.1 nm optical bandwidth, 170 μJ pulse energy, and a 10 Hz pulse rate. The beam was expanded using a cylindrical lens to evenly illuminate an area of approximately 1 cm x 1 cm on the imaging stage resulting in an energy density of about 1.76 J/m^2. The laser was mounted parallel to the stage and the beam directed via a steering mirror onto the sample at approximately 20° from the normal of the sample. A halogen lamp (150 W, Model I-150 Optical Fiber Light Source, Cuda) was used as the source for reflectance spectroscopy and was mounted 23° from the vertical axis and aligned to illuminate the specimen stage. This provided uniform illumination across a 2 cm x 2 cm imaging area.

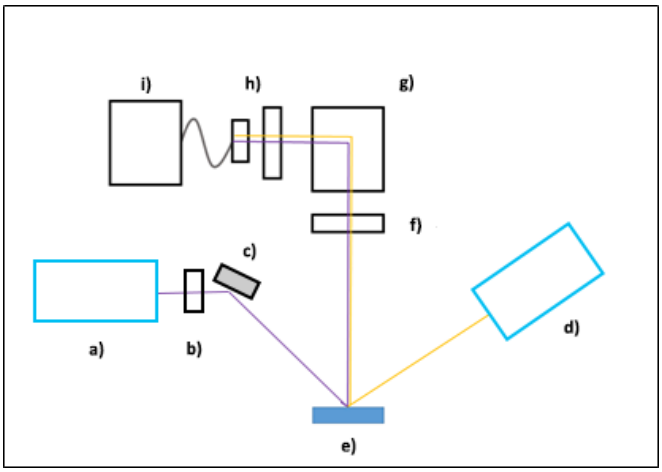

Figure 14: Schematic of the hyperspectral imaging system. The sample stage (e) is illuminated by either the nitrogen laser (a) focused through a cylindrical lens (b) and directed by a steering mirror (c) or by a halogen lamp (d). Light is collected from the sample by an imaging optic (f) and an image is formed on the DMD (g). The light is then reflected off the DMD's mirrors through a series of collection optics (h) and into a fiber where the signal is sent to a spectrometer (i).

To collect an image, a series of Hadamard matrices was programmed onto the DMD and a signal was collected for each code. The signal and the corresponding Hadamard code were saved for reconstruction, which occurred after all codes had been displayed. For the fluorescence imaging of the skin samples 3200 Hadamard patterns were used on the DMD with an integration time of 200 ms per code to acquire the intensity measurements needed to reconstruct the image. Total acquisition time was approximately 15 minutes. To obtain reflectance imaging of the liver and skin samples, 3200 Hadamard patterns were used with an integration time of 10 ms to acquire the intensity measurements needed to reconstruct the image. Total acquisition time was approximately 7 minutes. After image acquisition a MATLAB program based on the NESTA algorithm [36] was used to reconstruct the compressed images. This method of reconstruction was tested using a sample grid and was found to have a PSNR of about 19 dB per image and an RMSE of about 30.

Hyperspectral reflectance imaging of undamaged tissue samples was obtained by illuminating both liver and skin tissue samples with the halogen lamp. The skin samples were then illuminated with the nitrogen laser to obtain images of the autofluorescence of the tissue. A white light image was obtained for all samples using a traditional 8-megapixel CMOS array camera (iSight camera). These white light images do not contain spectral information. The morphology of structures seen in these white light images is compared to structures seen in the hyperspectral images.

After the initial images were obtained, the tissue samples were thermally damaged using an IPG Photonics thulium fiber laser at 1850 nm (TLM-5). Skin samples were illuminated for 35 seconds over a 0.78 mm^2 area with a power of 3 W. This created a thermally damaged region about 0.5 mm in diameter. Liver samples were illuminated for 60 seconds over a 1.1 mm^2 area with a power of 3 W, creating a thermally damaged region about 4 mm in diameter. The laser damage alters both the autofluorescence and reflectance spectra of the tissue. Reflectance HSI of both the damaged liver and skin samples was obtained and autofluorescence HSI of the damaged skin samples was acquired. An additional white light image of the damaged tissue was also obtained with the traditional array camera. After imaging was completed, the sizes of lesions on the liver samples were measured with a ruler, as the damaged region was clearly visible on these tissue samples.

3.3 Results and Analysis

3.3.1 Spectral Angle Mapping

The hyperspectral images were analyzed using the Spectral Angle Mapping or SAM algorithm.[42] SAM analysis compares a known reference spectrum to the spectrum of each pixel in a spectral image of an object to look for differences between the two, an example of which can be seen in figure 15. To create the reference spectrum, two wavelengths of interest are chosen and the intensities of all pixels in the reference image are determined in these two bands. These pixel intensities are graphed as a scatterplot and a linear regression is performed to define a reference vector. For comparison, a vector is created for each pixel in the image of the object. For each pixel, the intensity of the pixel in the two wavelength bands is plotted and the vector is drawn from the origin to this point. The reference and pixel vectors are then compared using the normalized dot product producing a spectral angle between the two vectors. This method is insensitive to differences in intensity since the SAM algorithm uses only the vector direction and not the vector length for comparison. This process can then be repeated for multiple wavelengths to create a hyperspectral angle.

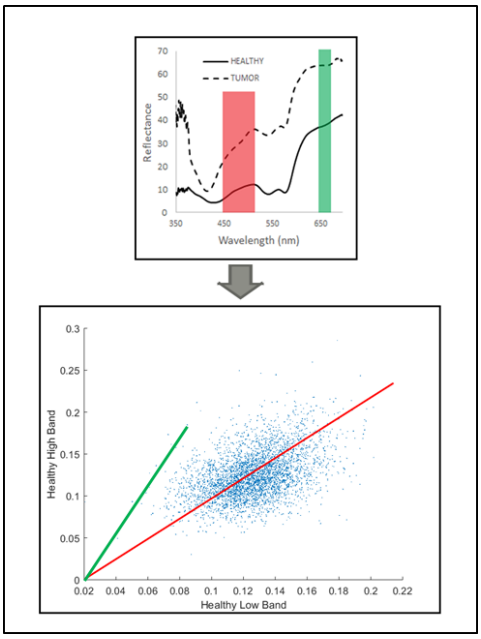

Figure 15: Panel a) An example of the process to create a spectral angle. To create the reference spectrum, two wavelength bands are chosen and the intensities of all pixels in the reference image are determined in these two bands. These pixel intensities are graphed as a scatterplot and a linear regression is performed to define a reference vector (red line). For comparison, a vector is created for each pixel in the image of the object. For each pixel, the intensity of the pixel in the two wavelength bands is plotted and the vector (green line) is drawn from the origin to this point. The reference and pixel vectors are then compared using the normalized dot product producing a spectral angle between the two vectors.

Figure 16 shows representative autofluorescence and reflectance spectra of healthy and thermally damaged porcine skin tissue. These spectra are shown to illustrate the changes in the spectra that result from thermal damage and the wavelength regions used for SAM analysis. The spectra of healthy tissue were created by taking the mean spectrum over a 9 x 9 pixel area in the image of the tissue taken before laser irradiation. The spectra of damaged tissue are the mean spectra across the region of thermal damage after laser irradiation. In the autofluorescence spectrum the dominant peak at 400 nm is collagen and the weaker peak near 425 nm is NAD(P)H. The collagen autofluorescent emission peak is stronger relative to the NAD(P)H peak for damaged tissue due to coagulation of collagen.

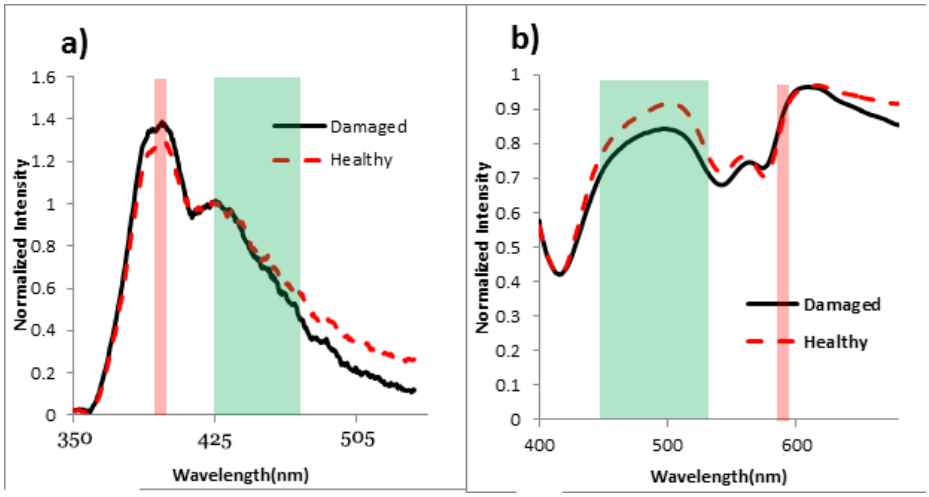

Figure 16: Panel a) The autofluorescence spectrum of porcine skin tissue before and after thermally damaging the tissue with an IR laser. The two fluorescence peaks of collagen (400nm) and NADPH (425 nm) are apparent in the undamaged spectra. The laser damage increased the collagen emission in the skin after illumination. Panel b) The reflectance spectrum of porcine skin tissue before and after illumination with the IR laser. In both panels the red and green regions indicate the wavelength ranges used to construct reference vectors for SAM analysis

A series of reference vectors was created using the hyperspectral images of undamaged porcine skin tissue. Separate reference vectors were created for each tissue sample. For the fluorescence images, the x-coordinate for all reference vectors was the average intensity over the 395-400 nm wavelength band in the image of undamaged tissue. The wavelength band used for the y-coordinate for the reference vectors was varied in 5 nm increments across the wavelength band 425-475 nm. This analysis resulted in a series of reference vectors across multiple wavelengths that were used to determine spectral angles when compared across the same wavelength ranges to images of tissue samples with thermal damage. Reference vectors for the reflectance images of healthy porcine skin were determined in a similar manner. The wavelength band 590-595 nm was used as the x-coordinate and the y-coordinate for the scatterplot was varied in 5 nm increments across the 450-520 nm band.

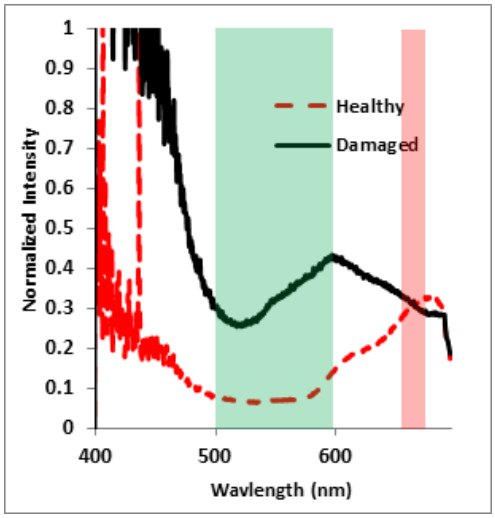

Figure 17: The reflectance spectrum of porcine liver tissue before and after thermally damaging the tissue with an IR laser. The red and green regions indicate the wavelength ranges used to construct reference vectors for SAM analysis.

Figure 17 shows a representative example of a reflectance spectrum of damaged and undamaged porcine liver tissue. The spectrum of healthy tissue was created by taking the mean spectrum over a 9 x 9 pixel area in the image of the tissue taken before laser irradiation. The spectrum of damaged tissue is the mean across the region of thermal damage after laser irradiation. To define the reference vectors for healthy porcine liver tissue, the intensities measured in the wavelength band 660 to 665 nm were used as the x-coordinate in the SAM scatterplot. The y-coordinate was varied in 5 nm increments across the 500 to 600 nm band.

3.3.2 SAM Analysis of Healthy Porcine Skin and Liver Tissue Samples

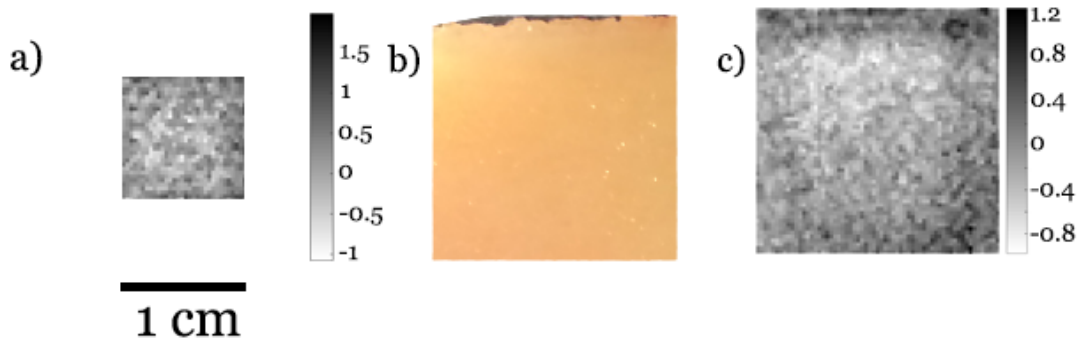

Figure 18: Panel a) An autofluorescence spectral angle image of porcine skin tissue before illumination with the IR laser. This image is a map of spectral angle, not intensity. The average of spectral angle in the illuminated region is 0.14 ± 0.47 degrees, indicating that the spectrum is uniform across the tissue sample. Panel b) A white light image of the same porcine skin sample. The tissue sample has a uniform appearance in this image. Panel c) A hyperspectral reflectance image of porcine skin tissue before illumination with the IR laser. This image is a map of spectral angle, not intensity. The average spectral angle is -0.42 ± 0.58 degrees, indicating that the spectrum is uniform across the tissue sample.

SAM analysis was applied to the images of healthy tissue. This analysis provides a measure of how uniform the spectra of the healthy tissue samples are as a function of position across the samples. A series of spectral angles was calculated for each reference vector and these spectral angles were summed to form a hyperspectral angle. Figure 18 shows representative examples of hyperspectral and white light images of healthy porcine skin tissue. The hyperspectral images are maps of the hyperspectral angle, not intensity. The white light image is a traditional intensity map and this white light image is uniform across the tissue sample. For the healthy tissue the spectral angle is approximately constant across the tissue, resulting in a uniform appearance in both the reflectance and fluorescence images. The spectral angle had an average value of 0.14 ± 0.47 degrees in the fluorescence image and -0.42 ± 0.58 degrees in the reflectance image. This indicates that the autofluorescence emission spectrum and the reflectance spectrum are approximately constant across the tissue sample.

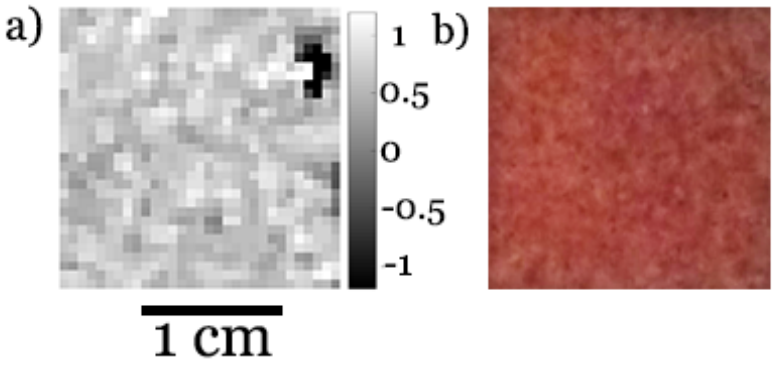

Figure 19: Panel a) A hyperspectral reflectance image of porcine liver tissue before illumination with the IR laser. This image is a map of spectral angle, not intensity. The dark spot in the upper right of the image is glare from the light source. The average of spectral angle in this image is 0.04 ± 0.32 degrees, indicating that the spectrum is uniform across the tissue sample. Panel b) A white light image of the same porcine liver sample. The appearance of the tissue is uniform across the tissue sample.

Figure 19 shows representative examples of hyperspectral and white light images of healthy porcine liver tissue. Again, the hyperspectral images are maps of the hyperspectral angle, not intensity. The white light image is a traditional intensity map and this white light image is uniform across the tissue sample. For the healthy tissue the spectral angle is approximately constant (0.04 ± 0.32 degrees) across the tissue, resulting in a uniform appearance in the reflectance images.

3.3.3 SAM Analysis of Thermally Damaged Porcine Skin Tissue Samples and Comparison to Healthy Tissue

Figure 20 shows a representative example of hyperspectral and white light images of thermally damaged porcine skin tissue. The hyperspectral images are maps of the hyperspectral angle, not intensity. The white light image is a map of intensity and thermal damage is clearly visible in these white light images. In both the autofluorescent and reflectance images, bright regions indicate areas in which the magnitude of the spectral angle is large. In both cases these bright areas correspond to the region of thermal

damage. The spectral angle has an average value of -2.29 ± 0.83 within the damaged region in the reflectance image and -4.29 ± 1.83 within the damaged region in the fluorescence image. In both cases the spectral angles are significantly different from the spectral angle of the healthy tissue. This large spectral angle indicates a significant change in the spectra of damaged tissue relative to healthy tissue.

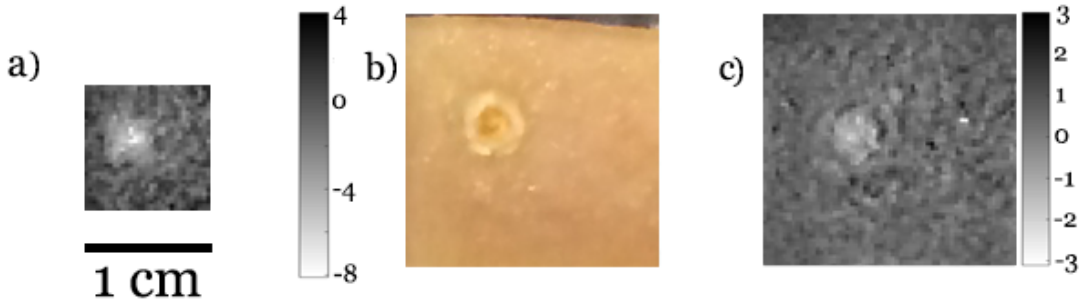

Figure 20: Panel a) A hyperspectral autofluorescence image of porcine skin tissue after illumination with the IR laser. This image is a map of spectral angle, not intensity. The bright spot in the center corresponds to a coagulation of collagen at the site of IR illumination. Panel b) A white light image of the same porcine skin sample with thermal damage clearly visible. Panel c) A hyperspectral reflectance image of porcine skin tissue after illumination with the IR laser. The bright spot in the center of the image corresponds to the damaged area.

The area of the damaged region as measured in the white light images was compared to the size of this region as measured in the hyperspectral images to see how well the hyperspectral imaging outlined the damaged regions. MATLAB was used to calculate the pixel area of the damaged region in all images. The boundary of the damaged region was determined by measuring the mean spectral angle of the entire image. Pixels with spectral angles greater than 1.5 standard deviations from this mean were considered to be part of the damaged region. A similar method using intensity values was used to determine the boundary of the damaged region in the white light images. The conversion from pixels to mm in the hyperspectral images was determined

by imaging a USAF resolution test plate and an object of known size was used as the basis of this conversion in the white light images.

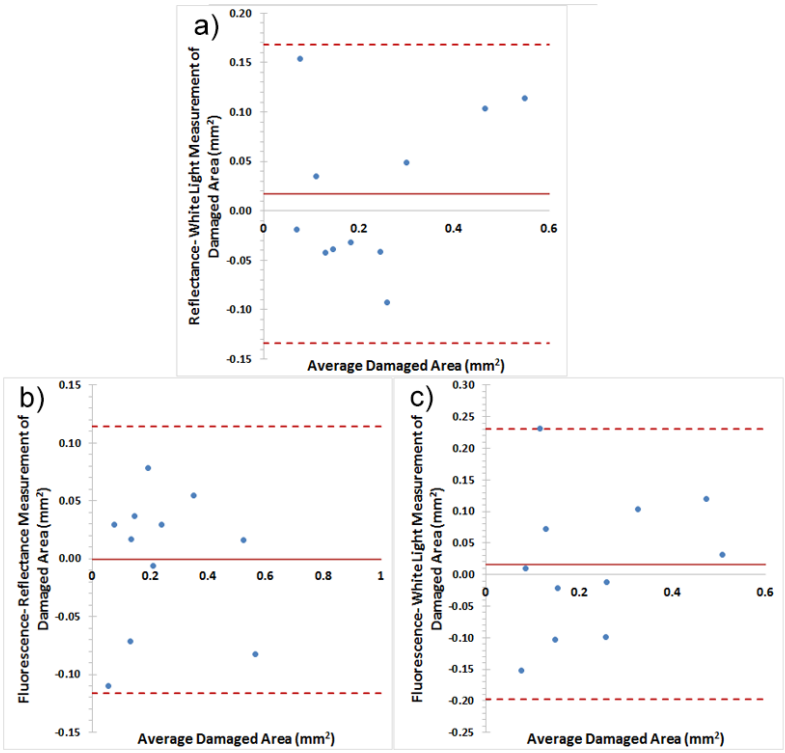

Figure 21: Bland-Altman plots comparing the areas of the thermally damaged regions as measured in the hyperspectral and white light images of porcine skin tissue. a) Comparison of the lesion areas in the reflectance and white light images. b) Comparison of the lesion areas in the autofluorescence and reflectance images. c) Comparison of the lesion areas in the autofluorescence and white light images.

Figure 21 shows Bland-Altman plots comparing the lesion areas measured in the white light and hyperspectral images. [43] Figure 21a shows good agreement between lesion areas as measured in the reflectance and white light images. All the measurements fall within two standard deviations of the mean difference and there is little difference between the bias and the line of equality. Figures 21b and 21c show similar relationships between the autofluorescence and reflectance images and autofluorescence and white light images, respectively. In all cases, these plots indicate good agreement between the

areas determined from the white light images and the hyperspectral images. This suggests that the hyperspectral technique is imaging the same region of thermal damage as is seen in the white light images. This indicates that the HSI system is sensitive to thermal damage of the tissue and can map the location of this damage.

3.3.4 SAM Analysis of Thermally Damaged Porcine Liver Tissue Samples and Comparison to Healthy Tissue

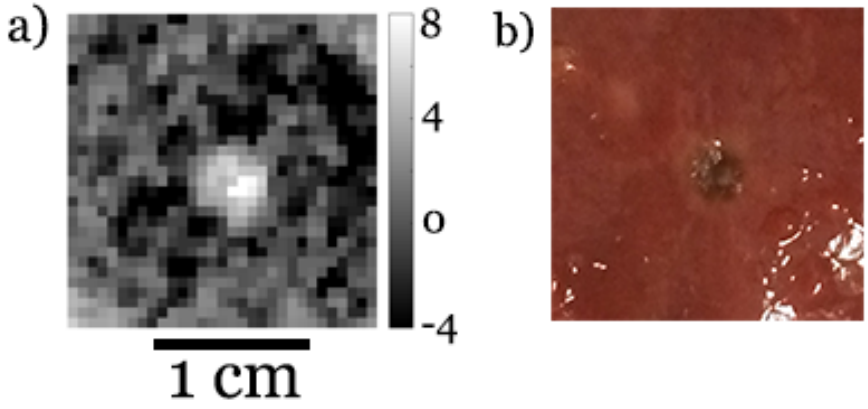

Figure 22: Panel a) A hyperspectral reflectance image of porcine liver tissue after illumination with the IR laser. This image is a map of spectral angle, not intensity. The bright spot corresponds to the damaged area on the liver tissue. Panel b) A white light image of the same porcine liver sample with thermal damage clearly visible.

Figure 22 shows a representative example of hyperspectral and white light images of thermally damaged porcine liver tissue. The hyperspectral images are maps of the hyperspectral angle, not intensity. The white light image is a map of intensity and thermal damage is clearly visible in these white light images. In the reflectance images, the bright region indicates an area in which the spectral angle is large, and this region corresponds to the location of thermal damage. This large spectral angle indicates a significant change in the reflectance spectrum of damaged tissue relative to healthy tissue. Using the same process described in section 3.3, the area of the damaged regions was measured in the

white light and hyperspectral images. The sizes of the damaged regions as measured in the white light images and the hyperspectral images were then compared. In addition, the size of the major axis of the lesion was measured with a ruler and the area was calculated assuming the lesion was a nearly circular ellipse. The reason for the ellipsoidal nature of the burn was due to the topology of the tissue. These measurements were also compared to the hyperspectral images.

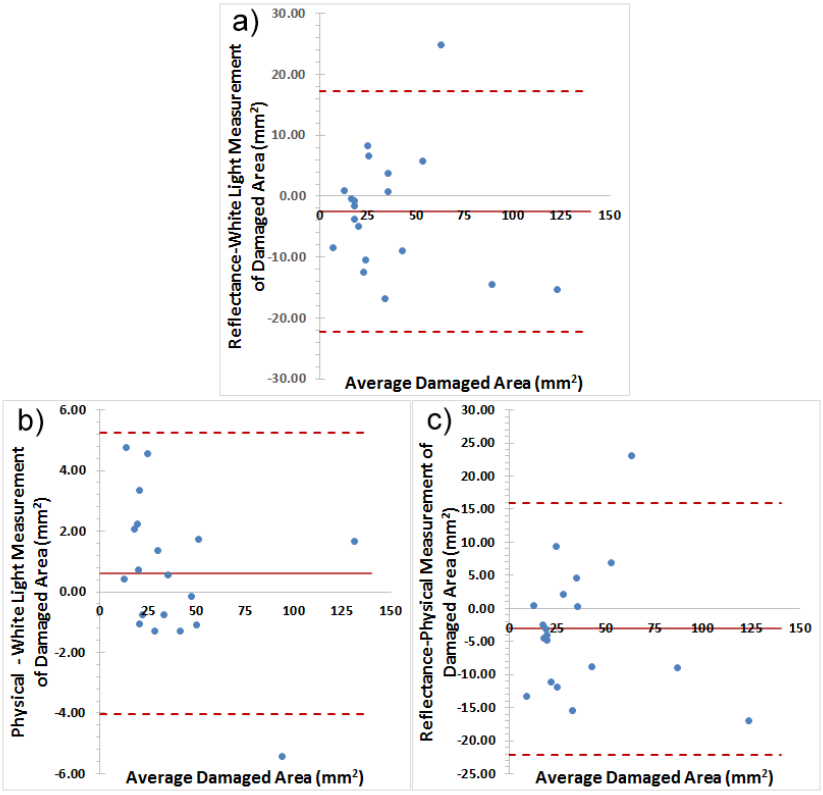

Figure 23: Bland-Altman plots comparing the areas of the thermally damaged regions as measured in the hyperspectral and white light images and via physical measurement for porcine liver tissue. a) Comparison of the lesion areas in the reflectance and white light images. b) Comparison of the lesion areas determined in the white light images and from physical measurement. c) Comparison of the lesion areas seen in the reflectance images and those determined from physical measurement.

Figure 23 shows Bland-Altman plots comparing the lesion areas measured in the white light and hyperspectral images and via physical measurement. [43] Figure 23a shows good agreement between lesion areas as measured in the reflectance and white light

images. All but one of the measurements fall within two standard deviations of the mean difference and there is little difference between the bias and the line of equality. Figures 23b and 23c show similar relationships between the physical measurement and white light images and the reflectance images and physical measurement, respectively. In all cases, these plots indicate good agreement between the areas determined from the white light images, hyperspectral images and physical measurement. This suggests that the hyperspectral technique is imaging the same region of thermal damage as is seen in the white light images and measured with the ruler. The HSI system is sensitive to thermal damage of the tissue and can map the location of this damage based on changes in the optical spectrum of the tissue.

3.4 Conclusions

A HSI system based on a single-pixel camera design for use in discriminating between healthy and unhealthy tissue based on the autofluorescence and reflectance spectra of the tissue has been constructed. Thermal lesions were created in ex vivo porcine skin tissue samples (n = 12) and porcine liver samples (n=15) using an IR laser. This thermal damage caused changes in the reflectance and autofluorescent spectra of the tissue. For the porcine skin samples, good agreement between the sizes of thermal lesions measured in both the autofluorescent and reflectance hyperspectral images and the lesion sizes measured via white light imaging are found. For the liver tissue, only reflectance imaging was obtained. Again, good agreement between lesion sizes measured in the hyperspectral reflectance images and sizes measured by both white light imaging and physical measurement is demonstrated. These studies show that the single-pixel HSI

system can differentiate between healthy and thermally damaged porcine skin and liver tissues.

The next step in testing the HSI system is to assess the ability of the HSI system to differentiate between healthy and cancerous tissue. The system currently takes about 15 minutes to collect a single image and this is clearly not “real-time” imaging. However, recently other groups have shown that single pixel compressive imaging can be made faster. G. Satat, et al have shown that by including time of flight data to the intensity measurements collected by the single pixel detector images can be reconstructed more accurately with fewer measurements. [44] The current limitation on acquisition time is hardware (both the speed of the DMD and computer) that can be overcome in future imaging systems.

4. Hyperspectral imaging based on compressive sensing to determine cancer margins in human pancreatic tissue ex vivo

4.1 Introduction

The American Cancer Society estimates that more than 1.6 million people will be diagnosed with cancer and over 600,000 will die from the disease in 2017. [45] While there have been great strides in the treatments of some cancers over the past decade, pancreatic cancer has maintained the lowest five year survival (7.8%) of all the major cancers monitored by the NIH [46] and the majority of these types of tumor are adenocarcinomas. Surgery remains the primary treatment for the majority of carcinoma, and other of solid mass tumors. The objective of surgery is to remove malignant tissue, while minimizing damage to adjacent healthy tissue to preserve function and/or for cosmetic reasons. A significant challenge for cancer surgery is ensuring that no residual malignant tissue is left behind as recurrent tumors lead to high mortality rates [47]. Consequently, the success of cancer surgery depends on a doctor's ability to visualize the margins of the tumor to be removed.

Multiple imaging modalities are available for preoperative tumor diagnosis and surgical planning, including x-ray, ultrasound, computed tomography (CT), magnetic resonance imaging (MRI), positron emission tomography (PET) and single photon emission computed tomography (SPECT). However, these techniques are not usually available during surgery. Paraffin section of inked surgical margins is the gold standard for margin assessment. Unfortunately, this process is time consuming and results are not available until several days after surgery. Typically, surgeons determine the tumor resection margins during procedures based on palpation, visual inspection and frozen

section histology. In some cases, intraoperative ultrasound is used to guide tissue excision [2]. Cancer surgeons need additional intraoperative imaging modalities for use during surgery to clearly delineate tumor margins and identify areas of residual disease**.**

Research has demonstrated that optical spectroscopy can be used to distinguish between healthy and diseased or damaged tissue. Both reflectance and fluorescence spectroscopy have been shown to effectively identify unhealthy tissue. [10-13] Autofluorescence emission is produced by the natural constituents of tissue (no exogenous fluorescent substances are added) when the tissue is illuminated by UV light. The autofluorescence of collagen, near 400 nm, and nicotinamide adenine dinucleotide phosphate, NAD(P)H, near 475 nm, have been noted for their high sensitivity to the presence of a range of different diseases.[7-9] The sensitivity arises because the autofluorescence spectra of proteins change due to alterations in the makeup and structure of unhealthy tissue compared to healthy tissue. Reflectance spectroscopy provides information about tissue morphology including cell size and density. Changes in the wavelength dependence of the reflected spectrum indicate differences in the morphology and/or make up of the tissue.[24]

HSI is a hybrid imaging modality that combines imaging and spectroscopy. By collecting spectral information at each position in a 2-D image, HSI generates a 3-D dataset of spatial and spectral information, known as a hypercube. Conventional HSI systems employ spatial or spectral scanning to acquire a hypercube.[24-25] Spatial scanning techniques obtain a spectrum in one location and then the object/spectrometer is translated to obtain spatial information. The full hyperspectral image is recovered after scanning is complete. In spectral scanning a 2-D image is projected through a tunable

filter or filter wheel and individual images are captured at different wavelengths. The hyperspectral image is reconstructed by combining the separate monochromatic images. Because HSI captures both spatial and spectral information, this technique has potential applications for noninvasive disease diagnosis and surgical guidance.

In this chapter, a HSI system based on a single-pixel camera design is used to examine the reflectance and autofluorescence spectra of pancreatic tissue to detect adenocarcinoma margins in tissue. A single pixel camera uses a single detector to create a 2-D image of a scene rather than using an array of detectors. [27] The primary advantage of this technique over other spectral imaging systems is its potential to function at low light levels. We aimed to detect changes in protein autofluorescence and reflectance due to the presence of malignant tissue and typically these signals are weak. The design and testing of this single-pixel HSI system is described in chapter 2 of this dissertation, but in this study the system is used to image malignant human tissue for the first time. This chapter presents the results of a 20 patient study comparing the ability of the HSI system versus visual tissue inspection augmented with traditional histology to delineate tumor margins in human pancreatic tissue imaged *ex vivo*.

4.2 Methods and Materials

Pancreatic tissue excised during pancreatectomy was imaged immediately after being sent to the pathology lab for analysis and before any processing or staining. After receiving the tissue sample, a pathologist sectioned the tissue into roughly 2 cm x 2 cm pieces and placed the 2-4 different sections into separate standard tissue embedding cassettes. These tissue samples were then imaged using the hyperspectral system. After

imaging, the samples were returned to the pathologist for processing and analysis. The hyperspectral imaging was later compared to the histological analysis. From the histology patients tissue was divided into three groups, wholly cancerous tissue, wholly healthy tissue, or tissue containing a margin. Some patients contributed tissue samples to multiple groups. The number of tissue samples from each group is shown in Table 1 below.

Table 1: The number of tissue samples from the 20 patients

Tissue Sample Type	Wholly Healthy Tissue	Wholly Cancerous Tissue	Margin
Number of tissue samples	12	10	19

In addition to the hyperspectral imaging, a white light image was obtained for all samples using a traditional 8-megapixel CMOS array camera (iSight camera). These white light images do not contain spectral information. The morphology of structures seen in these white light images was compared to structures seen in the hyperspectral images and in the histology slides.

The design and testing of a single-pixel hyperspectral imaging system for detecting changes in tissue properties has been previously reported by these authors. [19] In this study, this HSI system was used to image human pancreatic tissue *ex vivo*. Figure 1 shows a schematic of the HSI system. The digital micromirror device (DMD) in the system is a DLP5500 0.55″ XGA with 1024 x 768 pixels. The spectrometer is an Ocean Optics QE Pro Spectrometer (spectral range 350-750 nm, 1044 pixels in the linear array, and dispersion 0.335 nm/pixel). The spatial resolution of the system is set by the size of the pixels used in the binary codes used on the DMD. In this study, 32 x 32 Hadamard matrices were used on the DMD, with a FOV of 1.9 cm x 1.9 cm. The spatial resolution

was 0.44 mm/pixel. LabVIEW software was used to manipulate the DMD and capture the signal from the spectrometer.

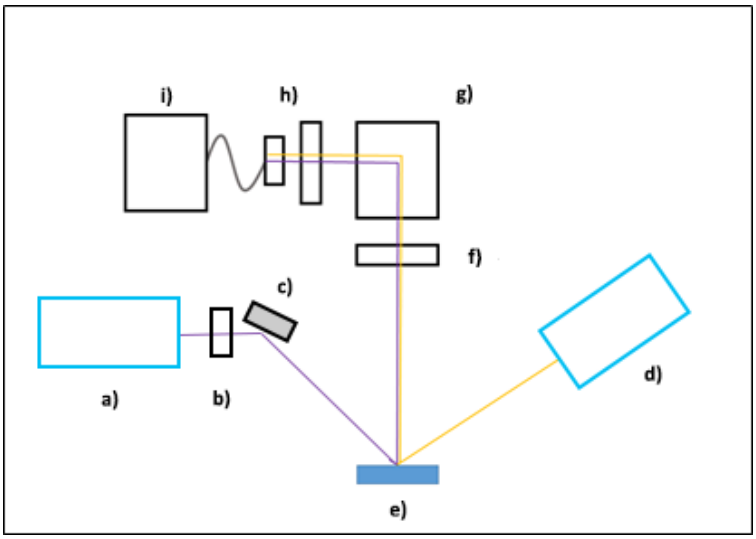

Figure 24: Schematic of the hyperspectral imaging system. The tissue sample in a histology cassette (e) is illuminated by either the nitrogen laser (a) focused through a cylindrical lens (b) and directed by a steering mirror (c) or by a halogen or xenon lamp (d). Light is collected from the sample by an imaging optic (f) and an image is formed on the DMD (g). The light is then reflected from the DMD's mirrors through a series of collection optics (h) and into a fiber where the signal is sent to a spectrometer(i).

The HSI imaging system was mounted on a vertical stage and imaged the tissue samples from above (see Figure 24). Either a halogen lamp (150 W, Model I-150 Optical Fiber Light Source, Cuda) or xenon (300 W, Circon MV 9086) source was used as the source for reflectance spectroscopy. Both light sources were mounted 23° from the vertical axis and aligned to illuminate the specimen. This provided uniform illumination across the 1.9 cm x 1.9 cm imaging area. A 3 mW nitrogen laser (SRS, NL100) was used as the excitation source for the autofluorescence spectroscopy and was mounted perpendicular to the imaging system. A steering mirror reflected the laser onto the sample and a cylindrical lens expanded the beam to provide uniform illumination over the tissue.

To collect an image, a series of Hadamard matrices was programmed onto the DMD and a signal was collected for each code. The signal and the corresponding Hadamard code were saved for reconstruction, which occurred after all codes had been displayed. To obtain reflectance, imaging 800 Hadamard patterns were used on the DMD with an integration time of 100 ms to acquire the intensity measurements needed to reconstruct the image. Total acquisition time was approximately 7 minutes. Because the fluorescence signal was much weaker than the reflectance signal, integration time for each Hadamard pattern was increased to 200 ms. Total acquisition time was approximately 15 minutes for each fluorescence image. After image acquisition a MATLAB program based on the NESTA algorithm was used to reconstruct the compressed images. [36]

4.3 Results and Analysis

4.3.1 Spectral Angle Mapping

The hyperspectral images were analyzed using the Spectral Angle Mapping (SAM) algorithm. [42] SAM analysis compares a known reference spectrum to the spectrum of each pixel in a spectral image of an object to look for differences between the two. To create the reference spectrum, two wavelengths of interest are chosen and the intensities of all pixels in the reference image are determined in these two bands. These pixel intensities are graphed as a scatterplot and a linear regression is performed to define a reference vector. For comparison, a vector is created for each pixel in the image of the object. For each pixel, the intensity of the pixel in the two wavelength bands is plotted and the vector is drawn from the origin to this point. The reference and pixel vectors are then compared using the normalized dot product producing a spectral angle between the

two vectors. This method is insensitive to differences in intensity since the SAM algorithm uses only the vector direction and not the vector length for comparison. This process can then be repeated for multiple wavelengths to create a hyperspectral angle.

4.3.2 Spectral Analysis of Pancreatic Tissue

Figure 25 shows the autofluorescence and reflectance spectra of pancreatic tissue to illustrate the differences between healthy and cancerous tissue. In the autofluorescence spectrum there are two dominant peaks. The peak at 400 nm is collagen and the peak near 455 nm is NAD(P)H. The collagen autofluorescence emission peak is stronger relative to the NAD(P)H peak for cancerous tissue due to fibrosis. The autofluorescence spectra of healthy and cancerous tissue are similar between 550-650nm, but differ significantly in the region around the collagen (375-400 nm) and NAD(P)H peaks (450-500nm). Absorption by blood (575 nm) is evident in the spectrum of the healthy tissue. The reflectance spectra of healthy and cancerous tissue are similar between 650 and 675 nm, but large differences are apparent from 450 to 520 nm. Scattering and absorption by hemoglobin (540 nm and 575 nm) are evident in the reflectance spectrum. There was significant variation in the appearance of healthy and cancerous tissue from patient to patient. Because of this reference vectors were determined on a patient-by-patient basis.

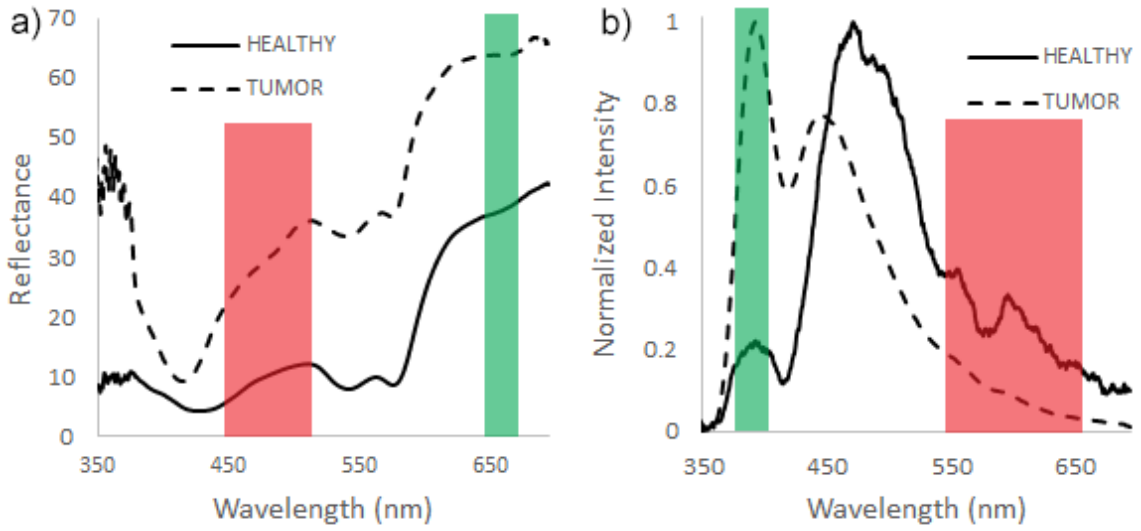

Figure 25: Panel a) The reflectance spectrum of healthy and cancerous pancreatic tissue. In both panels the red and green regions indicate the wavelength ranges used to construct reference vectors for SAM analysis. Panel b) The autofluorescence spectrum of healthy and cancerous pancreatic tissue. The two fluorescence peaks of collagen (~400nm) and NADPH (~450 nm) are apparent in the both spectra. The cancerous tissue has an increased collagen emission due to fibrosis associated with the tumor. The red and green regions indicate the wavelength ranges used to construct reference vectors for SAM analysis.

A series of reference vectors was created using the hyperspectral images of healthy pancreatic tissue. For the fluorescence images, the x-coordinate for all reference vectors was the average intensity over the 395-400 nm wavelength band in the image of undamaged tissue. This corresponds to the wavelength band over which the healthy and tumorous tissue spectra exhibit the largest difference across the collagen emission peak. The wavelength band used for the y-coordinate for the reference vectors was varied in 5 nm increments across the wavelength band 550-650 nm. This corresponded to the region across the NADPH autofluorescence peak over which the spectra of healthy and tumorous tissue are similar. This analysis resulted in a series of reference vectors across multiple wavelengths that were used to determine spectral angles when compared across the same wavelength ranges to images of tissue samples with a transition region from healthy to tumorous tissue.

Reference vectors for the reflectance images of healthy pancreatic tissue were determined in a similar manner. The wavelength band 650-655 nm was used as the x-coordinate and the y-coordinate for the scatterplot was varied in 5 nm increments across the 450-520 nm band.

4.3.3 SAM Reflectance Analysis of Healthy Pancreatic Tissue

Samples of healthy pancreatic tissue were obtained from 12 patients. These tissue samples did not contain any malignant tissue. We did not obtain samples of purely healthy tissue from all patients because in some cases regions of healthy tissue could not be identified by the pathologist due to the extent of disease. SAM analysis was applied to the images of healthy tissue to provide a measure of how uniform the spectra of the healthy tissue are as a function of position across the samples. A series of spectral angles was calculated for each reference vector and these spectral angles were summed to form a hyperspectral angle. Figure 26 (panels a and b) shows representative examples of white light and HSI of healthy pancreatic tissue. Some structures within the tissue are evident in the white light image. However, these structures are not seen in the HSI indicating that they have the same spectrum as healthy tissue. For the healthy tissue the spectral angle is approximately constant across the sample. The spectral angle has an average value of 0.98 ± 4.02 degrees in the reflectance images. This indicates that the reflectance spectra are approximately constant across the tissue samples.

Figure 26, panel c, identifies regions in the sample for which the spectral angle measured for the tissue was more than two standard deviations away from the spectral angle of the mean reference vector for healthy tissue. This was defined as the boundary condition between healthy and cancerous tissue. In these regions, HSI did not classify the

healthy tissue correctly. The specificity of the HSI method can be measured by determining the percentage of pixels that are properly classified as healthy in the images of healthy tissue. The average specificity for all HSI of healthy tissue was 83.90±5.09.

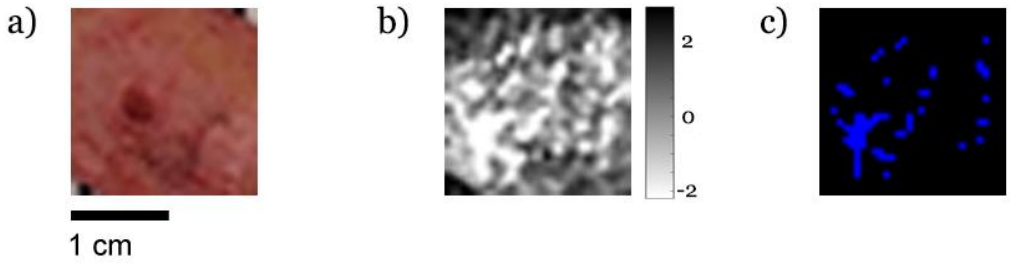

Figure 26: a) A white light image of healthy pancreatic tissue (no tumor present). The red circular structure near the center of the image is a blood vessel. b) The SAM image based on the HSI. The spectral angle is approximately uniform across the tissue. c) The blue pixels indicate regions for which the measured spectral angle is more than two standard deviations away from the mean reference spectrum.

4.3.4 SAM Reflectance Analysis of Malignant Pancreatic Tissue

Samples of malignant pancreatic tissue were obtained from 10 patients. These tissue samples contained only malignant tissue. We did not obtain samples of purely malignant tissue from the first 10 patients. SAM analysis was applied to the images of malignant tissue to access the ability if HSI to identify malignant tissue. In all cases, a series of reference vectors of healthy tissue were formed from a sample of healthy tissue for each patient. SAM analysis was then performed on the images of malignant tissue comparing the spectra in these images to the healthy tissue reference vector. Because all of the tissue in the samples was malignant, all pixels in the image should exhibit large spectral angles, indicating that the spectrum of the tissue was different from the healthy tissue spectrum. Figure 27 (panels a and b) shows representative examples of white light and HSI of malignant pancreatic tissue. Figure 27, panel c, identifies regions in the

sample for which the spectral angle measured for the tissue was more than two standard deviations away from the mean reference vector for healthy tissue. These are the pixels identified as malignant by HSI. The pixels that have smaller spectral angles have been classified as healthy tissue by HSI imaging. An average sensitivity of 75.42 ± 17.89 was found across this dataset.

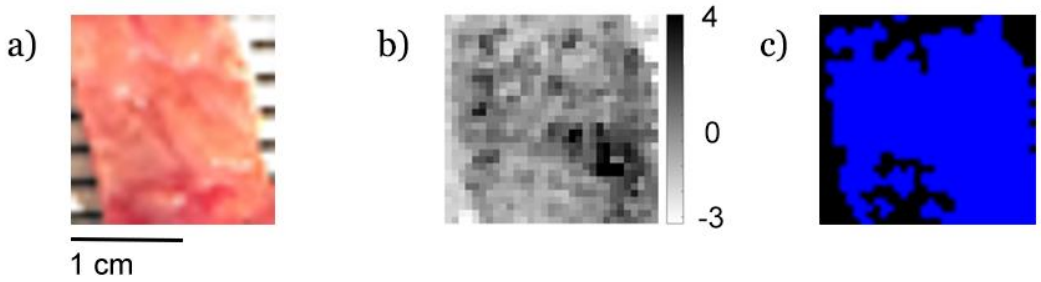

Figure 27: a*)* A white light image of a tissue sample that was entirely tumor. b) The reconstructed SAM image. c) The blue pixels indicate regions for which the measured spectral angle is more than two standard deviations away from the mean reference spectrum.

3.4 SAM Analysis of the Reflectance Spectra of Samples Containing both Healthy and Malignant Pancreatic Tissue

Tissue samples from 19 patients contained transition regions from healthy to cancerous tissue – a margin. SAM analysis was applied to these images, using the spectrum of healthy tissue as the reference vector. Figure 28 (panels a and b) shows representative examples of white light and HSI of a sample containing both healthy and malignant tissue. In the HSI, regions with large spectral angles are regions in which the spectrum of the tissue is significantly different from that of healthy tissue. Each HSI image was used with histology to denote regions in the tissue that were healthy or cancerous. Regions that were marked as "healthy" were used to create a binary mask that could be compared with the HSI. Regions in the HSI that were two standard deviations

away from the mean reference vector for healthy tissue were then identified as malignant. Comparing the two methods allowed a sensitivity and specificity to be found for each image. From this data a mean sensitivity of 74.80±9.18% and a specificity of 68.59±10.43% were determined.

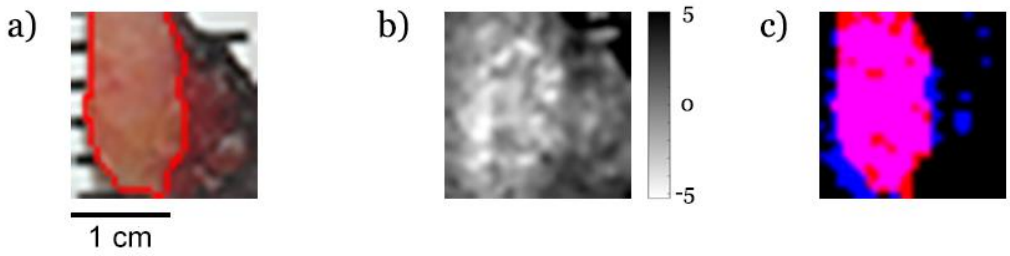

Figure 28: a) A white light image of pancreatic tissue. The red line denotes the border of the cancerous region. b) The reconstructed SAM image, the lighter color corresponds to a larger spectral angle indicting the presence of malignant tissue. c) A comparison of the pixels identified as malignant via HSI and via histology. The red pixels correspond to where histology found cancer, the blue pixels where HSI found cancer and purple where both imaging techniques detected cancer.

4.3.5 SAM Fluorescence Analysis of Pancreatic Tissue

The same process described in sections 3.3 and 3.4 was performed on fluorescence images of the tissue as well. The fluorescence signal of collagen and NAD(P)H are very faint and had a lower signal to noise then the reflectance images. For this reason, single pixel imaging's high dynamic range make it preferable to other imaging modalities. Unfortunately, the limitations to the project only allowed us to collect 3 fluorescence images. Those that did showed a promising ability to distinguish between healthy and cancerous tissue (Figure 29).

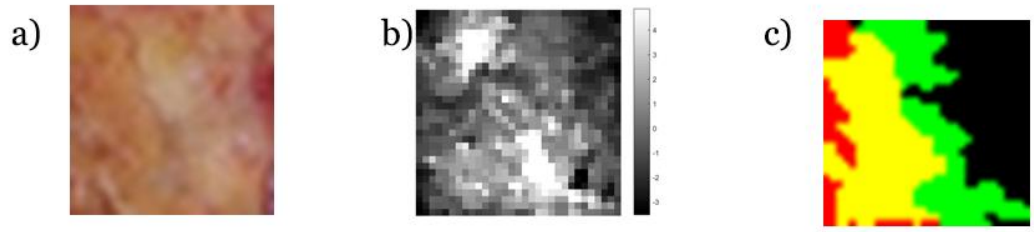

Figure 29: a) A white light image of pancreas the redder colored tissue that is dominant on the left side of the image is cancerous tissue. b) The reconstructed SAM image, the lighter color corresponds to a larger spectral angle from the reference vector calculated from healthy tissue. c) The masks of the cancerous tissue. The red pixels correspond to where histology found cancer, the green pixels where the reconstruction found cancer and yellow where both imaging techniques detected cancer.

4.4 Conclusions

A HSI system based on a single-pixel camera design for use in discriminating between healthy and malignant pancreatic tissue based on the autofluorescence and reflectance spectra of the tissue was constructed. Pancreatic tissue samples from 20 patients were imaged ex vivo using the single pixel HSI system. For the reflectance HSI a sensitivity of 74.80±9.18% and a specificity of 68.59±10.43% was determined. These results confirm that our camera is sensitive enough to detect spectral differences between healthy and malignant pancreatic tissue.

The system currently takes about 15 minutes to collect a single image which is insufficient for "real-time" imaging. However, recently other groups have shown that single pixel compressive imaging can be made faster. [44] The current limitation on acquisition time is hardware (both the speed of the DMD and computer) that can be overcome in future imaging systems. In addition, for this technology to be most useful in

an intraoperative setting, we will integrate HSI imaging into endoscopic and laparoscopic probes using a coherent fiber bundle.

Before this HSI technique can be used in a surgical setting the effects of blood profusion must be addressed. In the study presented the tissue was blotted and no blood was present on the surface of the tissue, however many groups have shown the presence of blood absorption effects the spectroscopy of tissue. [48] We will need to next test this technique on a live animal model to investigate these effects in more detail. The use of similar spectroscopic techniques has been shown to be effective in the detection of a range of different tumors [11-13]. Another avenue of potential development for this research is to test the camera's ability to detect tumor margins of skin and throat cancer.

5. Hyperspectral Compressive Polarization Imaging of Porcine Skin Tissue *Ex Vivo*

5.1 Introduction

As light interacts with a biological tissue via scattering and absorption, the reflectance spectrum changes. These changes in the reflectance spectrum provide information about tissue properties, including cell size and density, which can be used to distinguish healthy and unhealthy tissue. In previous chapters of this dissertation, this alteration of the reflectance spectrum resulting from the interaction of incident light and tissue was used to delineate the boundaries of thermal lesions and pancreatic tumors.

In addition to changes in the reflectance spectrum, as light travels through a biological tissue the polarization state of that light is altered. Examining the polarization of light to diagnose and mark damaged or diseased tissue has a long history in biomedical optics. Groups initially used illumination with polarized light to reduce glare from tissue surfaces. [49] Researchers soon discovered that polarized light could be used to increase the penetration depth and image superficial layers of tissue. [50] It was then found that cancerous tissue changed the birefengence in ways that made it possible to image and identify tumor margins. [51-52] Multi-spectral polarization imaging has been used to further refine the technique to identify specific chromophores. [53] Recent work done by Vasefi et al. has shown that combining the high spectral resolution of HSI with polarization imaging allows for the accurate selection of specific chromophores and markers in tissue.[54]

In this chapter, we discuss the addition of polarized light imaging to the single pixel HSI system that has been discussed in previous chapters. We use this system to measure

the polarization of back-scattered light from porcine skin samples (n=8). These samples were damaged with an IR laser and the sizes of the resulting lesions were measured using HSI polarization imaging, HSI reflectance imaging (the technique discussed in previous chapters) and white light imaging. The sizes of the lesions as measured using these three techniques are then compared.

5.2 Methods and Materials

The design and testing of a single-pixel hyperspectral imaging system for capable of detecting changes in tissue properties was discussed in previous chapters of this dissertation. This study uses the same HSI system as used in Chapters 3-4, with the addition of polarization imaging capabilities. In this study, 64 x 64 Hadamard matrices were used on the DMD, with a FOV of 1.9 cm x 1.9 cm. The spatial resolution was 0.30 mm/pixel.

The imaging system was mounted on a vertical stage and imaged a sample stage (see Figure 30). A xenon (300 W, Circon MV 9086) source was used as the source for reflectance spectroscopy and was mounted 23° from the vertical axis and aligned to illuminate the specimen stage. The light from the xenon source was passed through a linear polarizer (Thorlabs LPVISE100-A). This provided uniform polarized light illumination across the 2 cm x 2 cm imaging area. A second linear polarizer was placed after the DMD, to act as an analyzer.

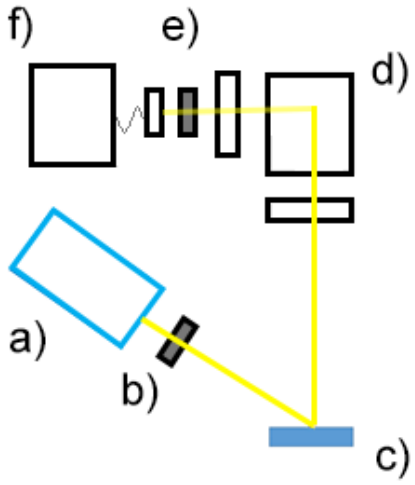

Figure 30: Schematic of the hyperspectral imaging system. The porcine sample (c) is illuminated by polarized light that comes from a halogen lamp (a) after passing through a linear polarizer. Light is collected from the sample by an imaging optic and an image is formed on the DMD (d). The light is then reflected off the DMD's mirrors through a series of collection optics and passes through an analyzer. (e) The light is then collected by a fiber where the signal is sent to a spectrometer. (f)

The tissue was imaged at four different orientations of the analyzer (0°,45°,90°,135°) to allow for the reconstruction of the polarization intensity. To collect an image for each position of the analyzer, a series of 3200 Hadamard matrices was programmed onto the DMD and a signal was collected for each code. The signal and the corresponding Hadamard code were saved for reconstruction, which occurred after all codes had been displayed. The analyzer was then adjusted to the next polarization angle and the process was repeated to obtain 4 images. To obtain reflectance imaging, the four images were summed together. Total acquisition time was approximately 15 minute per image, and about an hour per sample. After image acquisition a MATLAB program based on the NESTA algorithm [36] was used to reconstruct the compressed images. A white light image was obtained for all samples using a traditional 8-megapixel CMOS array camera (iSight camera). The morphology of structures seen in these white light images is compared to structures seen in the hyperspectral images.

For this *ex vivo* study, porcine skin tissue samples (n=8) of uniform thickness were cut into 2 cm x 2 cm squares. Polarized light HSI, reflectance HSI and white light imaging was obtained of all samples. After the initial images of healthy tissue were obtained, the tissue samples were thermally damaged using an IPG Photonics Nd:YAG laser at 1064 nm. Skin samples were illuminated for about 3 minutes over a 10 mm^2 area with a power of 1 W. This created a thermally damaged region about 4 mm in diameter. The damaged samples were then imaged using the three techniques.

5.3 Results and Analysis

5.3.1 Reflectance HSI and White Light Images of Healthy and Damaged Tissue

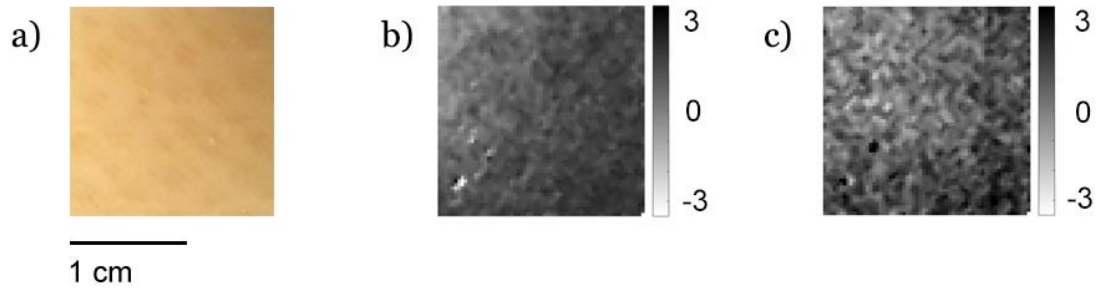

Figure 31: Panel a) A white light image of healthy porcine tissue Panel b) The HSI reflectance SAM image, the lighter color corresponds to a larger spectral angle from the reference vector calculated from healthy tissue. Panel c) The polarized light HSI SAM image.

Figure 31 panel a shows the white light image of a representative example of a healthy porcine skin sample. The white light image is a traditional intensity map. The tissue is uniform in appearance. Figure 33 panel a shows the white light image of a tissue sample after laser irradiation. A region of thermal damage is evident near the center of the image.

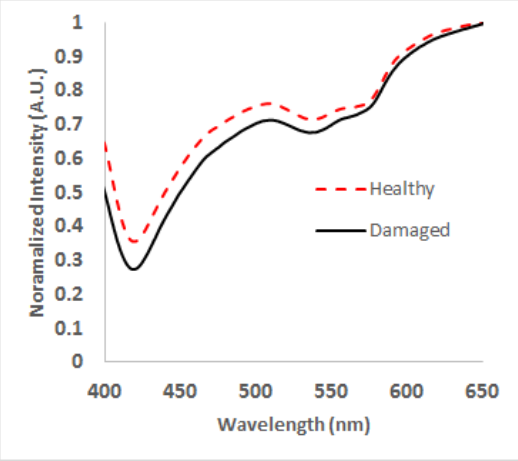

Figure 32: The reflectance spectrum of porcine skin tissue before and after illumination with the IR laser. Because a different laser source was used in this study the change in the spectrum is not as pronounced as the change seen in Chapter 3.

Figure 32 shows the reflectance spectrum of healthy and thermally damaged tissue. These spectra are shown to illustrate the changes in the spectrum that result from thermal damage. The spectrum of healthy tissue was created by taking the mean spectrum over a 60 x 60 pixel area in the image of the tissue taken before laser irradiation. The spectrum of damaged tissue is the mean across the region of thermal damage after laser irradiation. The change in the spectrum after laser irradiation is not as pronounced as that seen in the earlier studies described in Chapter 3. This is because we used a different laser source (1064 nm) to create the thermal damage in this study. This 1064 nm laser has a larger penetration depth than the 1850 nm laser used previously. As a result, the laser energy was spread over a larger volume in the tissue, resulting in less heating and less thermal damage.

SAM analysis was applied to the HSI reflectance imaging of both healthy and damaged tissue using the methods previously discussed in Chapters 3 and 4. Separate reference vectors for healthy tissue were created for each tissue sample. The x-coordinate

for all reference vectors was the average intensity over the 600-605 nm wavelength band in the images of undamaged tissue. The wavelength band used for the y-coordinate for the reference vectors was varied in 5 nm increments across the wavelength band 460-550 nm. A series of spectral angles was calculated for each image. Figure 31, panel b shows a representative example of the hyperspectral reflectance SAM image of healthy porcine skin tissue. The spectral angle is approximately constant across the tissue, resulting in a uniform appearance in the reflectance image. The spectral angle had an average value of 0.22 ± 0.28 degrees in the reflectance images. These results indicate that the reflectance spectrum is approximately constant across the tissue sample before illumination with the laser. Figure 33, panel b shows a shows representative example of the hyperspectral reflectance SAM image of thermally damaged porcine skin tissue. The bright region near the center of the image is a region in which the magnitude of the spectral angle is large, and this region corresponds to the region of thermal damage. The spectral angle has an average value of -2.98 ± 0.85 within the damaged region in the reflectance image. The spectral angle in the damaged region is significantly different from the spectral angle of the healthy tissue. This indicates a change in the spectrum of the damaged tissue relative to healthy tissue.

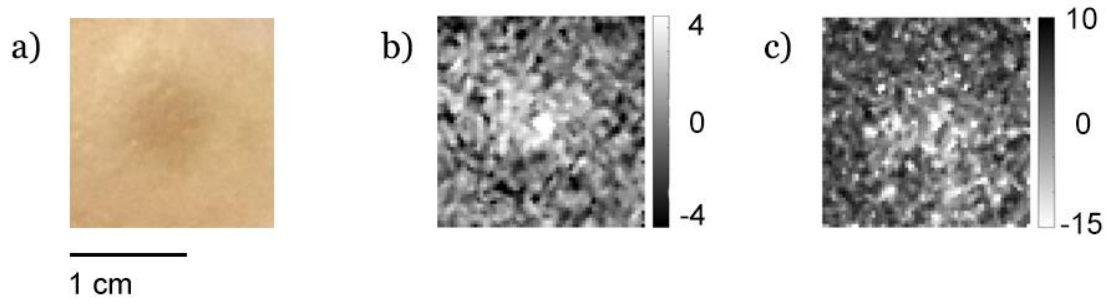

Figure 33: Panel a) A white light image of the same porcine skin sample with thermal damage clearly visible. Panel b) A hyperspectral reflectance image of porcine skin tissue after illumination with the IR laser. The bright spot in the center corresponds to a coagulation of collagen at the site of IR illumination. Panel c) A hyperspectral polarization image of porcine skin tissue after illumination with the IR laser. The bright spot in the center of the image corresponds to the damaged area.

MATLAB was used to calculate the pixel area of the damaged region in both the HSI reflectance and white light images. For the HSI, the boundary of the damaged region was determined by measuring the mean spectral angle of the entire image. Pixels with spectral angles greater than 2 standard deviations from this mean were considered to be part of the damaged region. A similar method using intensity values was used to determine the boundary of the damaged region in the white light images.

5.3.2 Polarized Light HSI of Healthy and Damaged Tissue

The images reconstructed at four different orientations of the analyzer (Im_0, Im_{45}, Im_{90}, Im_{135}) were used to create a polarization image. The images were combined to create hyperspectral images of the Stokes parameters Q and U using equations 1 and 2. These two images of the Stokes parameters were then used to create an HSI of the linear polarization (Pol) using equation 3.

$$Q = \frac{Im_0 - Im_{90}}{Im_0 + Im_{90}} \quad \textbf{(equation 1)}$$

$$U = \frac{Im_{45} - Im_{135}}{Im_{45} + Im_{135}} \quad \textbf{(equation 2)}$$

$$Im_{POL} = \sqrt{Q^2 + U^2} \quad \textbf{(equation 3)}$$

The Im_{pol} is a hypercube of linear polarization as function of position and wavelength across the tissue sample. The tissue is illuminated with 100% linearly polarized light. If the tissue does not depolarize the light via multiple scatterings, you would expect to detect 100% polarized light. A drop in the percentage of polarization then is likely due to scattering of light in the tissue.

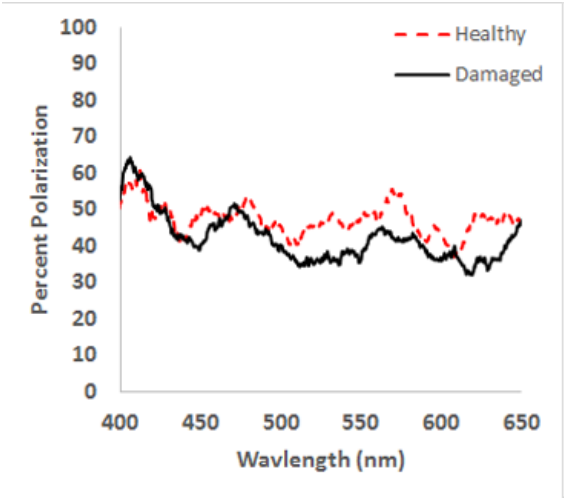

Figure 34: The polarization spectrum of porcine skin tissue before and after thermally damaging the tissue with an IR laser. The polarization remains constant at lower wavelengths while damaging with the laser depolarizes the tissue at higher wavelengths.

Figure 34 shows the polarization as a function of wavelength of both healthy and damaged tissue. The healthy tissue polarization spectrum was created by taking the mean spectrum over a 60 x 60 pixel area in the image of the tissue before laser irradiation. The polarized light spectrum of damaged tissue is the mean spectrum across the region of thermal damage. The polarization of healthy tissue is relatively constant over the spectrum. After damaging with the laser, the polarization changes. At shorter

wavelengths, from about 400-475 nm, there is little variation from the healthy tissue. From 500-650 nm the damaged tissue has lower polarization compared to healthy tissue, this is due to a change in the scattering properties of the damaged tissue.

The polarized light HSI spectral images were then analyzed using the SAM algorithm as previously discussed in Chapters 3 and 4.[42] Separate reference vectors for healthy tissue were created for each tissue sample. The x-coordinate for all reference vectors was the average intensity over the 405-410 nm wavelength band in the images of undamaged tissue. The wavelength band used for the y-coordinate for the reference vectors was varied in 5 nm increments across the wavelength band 500-650 nm. This analysis resulted in a series of reference vectors across multiple wavelengths that were used to determine spectral angles relative to the healthy tissue reference vector.

Figure 30 panel c shows a representative example of a SAM image of polarized light HSI of healthy porcine skin tissue. The spectral angle is approximately constant across the tissue. The spectral angle had an average value of -0.32 ± 0.66 degrees in the polarized light HSI. These results indicate that the polarization spectrum is approximately constant across the tissue sample before illumination with the laser.

Figure 32 panel c shows a representative example of a SAM image of polarized light HSI of thermally damaged porcine skin tissue. The bright regions near the center of the image indicate areas in which the magnitude of the spectral angle is large. These bright areas correspond to the region of thermal damage. The spectral angle has an average value of 3.54 ± 1.57 within the damaged region in the polarized light image. In the spectral angles are different from the spectral angle of the healthy tissue. This large spectral angle indicates a change in the polarization as a function of wavelength of

damaged tissue relative to healthy tissue, which suggests a change in the scattering properties of the tissue.

MATLAB was used to calculate the pixel area of the damaged region in the polarized light HSI. The boundary of the damaged region was determined by measuring the mean spectral angle of the entire image. Pixels with spectral angles greater than 2 standard deviations from this mean were considered to be part of the damaged region.

5.3.3. Comparison of Polarized Light HSI to White Light and Reflectance HSI

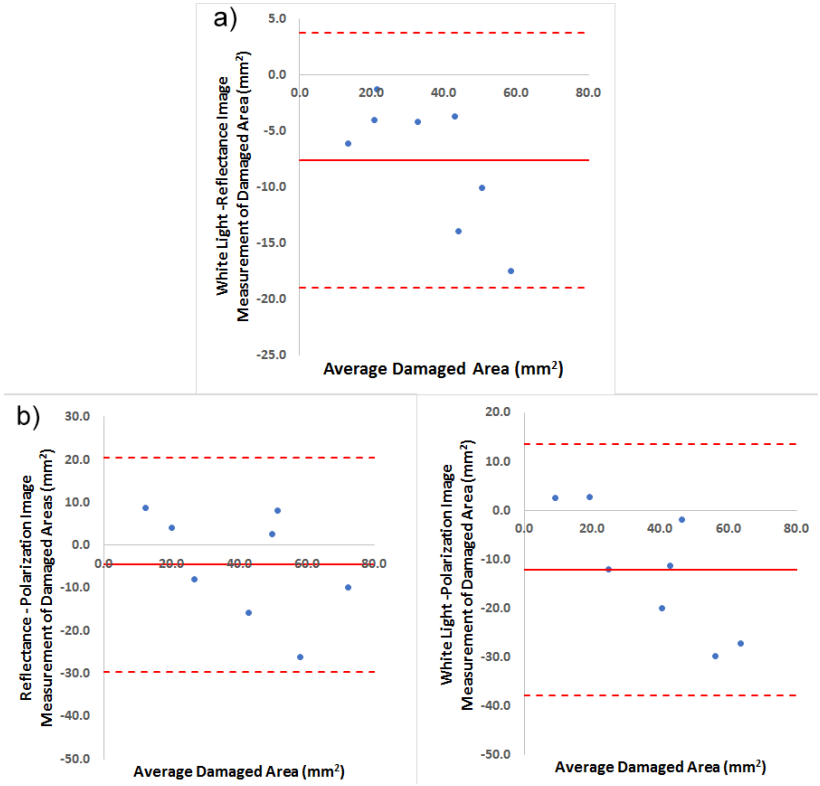

Figure 35: Bland-Altman plots comparing the areas of the thermally damaged regions as measured in the polarized light HSI, reflectance HSI and white light images of porcine skin tissue. a) Comparison of the lesion areas in the white light images and reflectance HSI. b) Comparison of the lesion areas in the reflectance HSI and polarized light HSI. c) Comparison of the lesion areas in the white light images and polarized light HSI.

Figure 35 shows Bland-Altman plots comparing the lesion areas measured in the white light, reflectance HSI and polarized light HSI. Figure 34a shows good agreement between lesion areas as measured in the reflectance HSI and white light images. This is consistent with the finding in Chapter 3. All the measurements fall within two standard deviations of the mean difference and there is little difference between the bias and the line of equality. Figures 35b and 35c show similar relationships between the polarized light and reflectance HSI and the white light images and polarized light HSI, respectively. In all cases, these plots indicate good agreement between the areas determined from polarized light HSI, white light images and the reflectance HSI. This suggests that the polarized light HSI is sensitive to thermal damage of the tissue and can map the location of this damage.

5.4 Conclusions

A HSI system based on a single-pixel camera design for use in discriminating between healthy and unhealthy tissue based on the linear polarization and reflectance spectra of the tissue has been constructed. Thermal lesions were created in *ex vivo* porcine skin tissue samples (n = 8) using an IR laser. This thermal damage caused changes in the reflectance and polarization spectra of the tissue. For the porcine skin samples, good agreement between the sizes of thermal lesions measured in both the polarization and reflectance hyperspectral images and the lesion sizes measured via white light imaging are found. These studies show that the single-pixel HSI system is sensitive to the changes in polarization as a function of wavelength produced by thermal damage.

This test has shown the systems potential in capturing polarized light HSI. The next step in testing this imaging modality to attempt to reproduce results by prior groups. As mentioned in the introduction of this chapter, Jacque et al, used polarization imaging to image light from superficial layers of tissue and groups have used both broadband and multispectral polarization to detect damaged tissue boundaries, [52,53] both techniques could be performed with this system as well.

These studies show the technique described in this chapter has the sensitivity to detect differences in tissue properties. As shown in chapter 4 of this dissertation, cancer changes the properties of the tissue. It may be possible to enhance the sensitivity of the system presented in chapter 4 by adding polarization imaging to it. Research has also shown that the polarization of fluorescence can be used to enhance cancer imaging [53], this suggests such a technique may increase the sensitivity of the fluorescence measurements presented in 4.3.5.

The effectiveness of those techniques in comparison to reflectance and autofluorescence measurements described in earlier chapters needs to be quantified as well. While the study presented here demonstrates the sensitivity of the system to polarization it does not demonstrate whether polarization imaging presents a better measurement of tissue damage then reflectance imaging alone. A further study needs to be undertaken with comparisons to histology to demonstrate the accuracy of the technique.

6. Conclusions

The overall goal of this study was to develop a hyperspectral imaging camera that can be used in the operating room to detect the boundaries between healthy tissue and tumors. The study was divided into 4 experiments each designed to test the HSI camera's abilities.

In chapter 2 the design and testing of the initial single pixel imaging camera was discussed. The camera was built, and a series of test images were used to measure the spectral and spatial resolution. The samples were imaged in fluorescence and reflectance modes simulating future study conditions. The compressive error was also tested and relations between image reconstruction quality and the number of Hadamard codes sent to the DMD were quantified. Using this information, the camera's operating parameters were determined for future studies.

In chapter 3 the camera's ability to detect changes in tissue properties were first investigated. Porcine skin and liver tissues were imaged before and after being thermally damaged creating a lesion. The tissue was imaged in fluorescence and reflectance modes and the size of the lesion were compared to white light images and physical measurements. These results confirmed the sensitivity of the camera to changes in tissue properties using reflectance imaging. Fluorescence imaging was found to be effective as well in determining lesion size in skin tissue, however the blood perfusion in the liver tissue quenched the fluorescence signal in these samples. A very faint signal was detected from the liver tissue, however the instability in the laser source combined with the absorption of the blood prevented this signal from being successfully reconstructed.

Recent advances in characterizing and removing blood spectra [56-57] along with a constant laser source suggest this method could be possible in future studies.

In chapter 4 the camera was used to detect the boundaries between cancerous and healthy tissue in human pancreatic tissue. Twenty patients pancreatic tissue was imaged, and the images were compared to white light images augmented with histology. An overall sensitivity of 74.80±9.18% and a specificity of 68.59±10.43% was found which confirms our systems sensitivity to the changes in tissue caused by the presence of solid mass tumors. Previous research has found reflectance spectroscopy has lower sensitivity than fluorescent spectroscopy due to differences in bulk tissue composition for single samples. [16-17] The lower than expected specificity of the images were hypothesized to be a combination of low spatial resolution and compression error. Increasing the spatial resolution while maintaining the same field of view requires hardware upgrades to the system, and new and efficient compression algorithms offer quicker acquisition and lower compression error. [58]

In chapter 5 the camera was augmented with linear polarizers to explore the possibility of adding polarization imaging to the camera. A similar experiment to the one described in chapter 3 was conducted and polarization intensity images were compared to reflectance and white light images. These results confirmed the sensitivity of the camera to changes in the tissues polarization properties as well as those previously explored. Adding this extra layer of information to the camera will help increase the accuracy of the camera and hopefully increase the reliability of the system.

The camera system presented in this dissertation has now been shown to be sensitive to a variety of spectroscopic signals from tissue - fluorescence, reflectance, and

polarization. The goal of the project was to develop the hyperspectral camera to be used in a surgical setting, and at the end of this dissertation the camera has shown significant progress to this goal. However, additional studies will need to pursue several avenues before the system is ready for a surgical setting. The reliability of the system needs to be experimentally tested before it is ready for a medical setting, this includes upgrading several hardware pieces on the system including the light source and DMD improving speed and sensitivity.

Once these tests have been performed a fourth and easily accessible imaging modality that can be added to the system is fluorescence polarization, which has been shown to be useful in delineating certain types of cancer. [59] The systems sensitivity has been tested on pancreatic cancer, melanoma and skin cancer has shown in the literature to have similar signatures [54,59] that suggest our system would excel at this type of imaging. Finally, discussions with surgeons at CMC have also highlighted a desire to deliver the imaging system through an endoscopic system. A fiber-based system would allow it to be delivered into a variety of surgical options and open a range of diseases that may be investigated with this tool.

References

1. Butcher L. Solid Tumors: Prevalence, Economics, And Implications for Payers and Purchasers. Biotechnology healthcare. 2008;5(1):20-21.
2. Cleary, Kevin and Peters, Terry M. (2010) Image-Guided Interventions: Technology Review and Clinical Applications Annual Review of Biomedical Engineering 2010 12:1, 119-142
3. Spiro RH, Guillamondegui O, Paulino AF, et al. Pattern of invasion and margin assessment in patients with oral tongue cancer. Head & Neck. 1999; 21(5):408–413
4. Bransden B.H, Joachain,C.J., Physics of Atoms and Molecules,Logman Scientific & technical, 1988, Logman Group Limited
5. Joseph R. Lakowicz, Principles of Fluorescence Spectroscopy, 3rd edition, 2003, Springer Science Business Media
6. Nelson, B. K., Cai, X. and Nebenführ, A. (2007), A multicolored set of in vivo organelle markers for co-localization studies in Arabidopsis and other plants. The Plant Journal, 51: 1126–1136.
7. Ramanujam N., Mitchell M., Mahadevan A., Warren S., Thomsen S., Silva E., Richards-Kortum R. In vivo diagnosis of cervical intraepithelial neoplasia using 337-nm-excited laser-induced fluorescence. Proc. Natl. Acad. Sci. USA, 91: 10193-10197, 1994
8. Cothren RM, Richards-Kortum R, Sivak MV, Jr, Fitzmaurice M, Rava RP, Boyce GA, Doxtader M, Blackman R, Ivanc TB, Hayes GB, et al. Gastrointestinal tissue diagnosis by laser-induced fluorescence spectroscopy at endoscopy. Gastrointest Endosc. 1990 Mar-Apr;36(2):105–111

9. Schomacker KT, Frisoli JK, Compton CC, Flotte TJ, Richter JM, Nishioka NS, Deutsch TF. Ultraviolet laser-induced fluorescence of colonic tissue: basic biology and diagnostic potential. Lasers Surg Med. 1992;12(1):63–78
10. Z. Volynskaya, A. S. Haka, K. L. Bechtel, M. Fitzmaurice, R. Shenk, N. Wang, J. Nazemi, R. R. Dasari, and M. S. Feld, "Diagnosing breast cancer using diffuse reflectance spectroscopy and intrinsic fluorescence spectroscopy," J. Biomed. Opt. 13(2), 024012 (2008).
11. G. Zonios, L. T. Perelman, V. Backman, R. Manoharan, M. Fitzmaurice, J. V Dam, and M. S. Feld, "Diffuse reflectance spectroscopy of human adenomatous colon polyps in vivo," Appl. Opt. 38(31), 6628–6637 (1999).
12. S. K. Chang, N. Marin, M. Follen, and R. Richards-Kortum, "Model-based analysis of clinical fluorescence spectroscopy for in vivo detection of cervical intraepithelial dysplasia," J. Biomed. Opt. 11(2), 024008 (2006).
13. I. Georgakoudi, and M. S. Feld, "The combined use of fluorescence, reflectance, and light-scattering spectroscopy for evaluating dysplasia in Barretts esophagus," Gastrointest. Endosc. Clin. N. Am. 14(3), 519–537, ix (2004).
14. Chandra M, Scheiman J, Simeone D, McKenna B, Purdy J, Mycek M; Spectral areas and ratios classifier algorithm for pancreatic tissue classification using optical spectroscopy. J. Biomed. Opt. 0001;15(1):010514-010514-3
15. Malavika Chandra et all , Pancreatic tissue assessment using fluorescence and reflectance spectroscopy, 2007

16. Johnson KS, Chicken DW, Pickard DO, et al; Elastic scattering spectroscopy for intraoperative determination of sentinel lymph node status in the breast. J. Biomed. Opt. 0001;9(6):1122-1128.
17. Chandra M., Scheiman J., Heidt D., Simeone D., McKenna B., Mycek M.-A., "Probing pancreatic disease using tissue optical spectroscopy," J. Biomed. Opt. 12(6), 060501 (2007).10.1117/1.2818029
18. Volynskaya Z, Haka A S, Bechtel K Diagnosing breast cancer using diffuse reflectance spectroscopy and intrinsic fluorescence spectroscopy, Journal of Biomedical Optics 132, 024012 March/April 2008
19. Howlader N, Noone AM, Krapcho M, Garshell J, Miller D, Altekruse SF, Kosary CL, Yu M, Ruhl J, Tatalovich Z,Mariotto A, Lewis DR, Chen HS, Feuer EJ, Cronin KA (eds). SEER Cancer Statistics Review, 1975-2012, National Cancer Institute. Bethesda,
20. WHIPPLE PROCEDURE (PANCREATICODUODENECTOMY), Pancreatic Cancer Action Network, https://www.pancan.org/section-facing-pancreatic-cancer/learn-about-pan-cancer/treatment/surgery/whipple-procedure-pancreaticoduodenectomy/
21. Verbeke C, Menon K, Redefining resection margin status in pancreatic cancer,HPB (Oxford). 2009 Jun; 11(4): 282–289
22. Chang D, Johns A, et all. Margin Clearance and Outcome in Resected Pancreatic Cancer, JCO June 10, 2009 vol. 27 no. 17 2855-2862
23. Polder, Gerrit & Pekkeriet, Erik & Snikkers, Marco. (2013). A Spectral Imaging System for Detection of Botrytis in Greenhouses.

24. Wallace, MB, Backman, V, Perelman, LT, Crawford, JM, Fitzmaurice, M, Seiler, M, Badizadegan, K, Shields, SJ, Itzkan, I, Dasari, RR, Van Dam, J, and Feld, MS. "Endoscopic detection of dysplasia in patients with Barrett's esophagus using light-scattering spectroscopy," Gastroenterology. 119: 677–682 (2000).
25. Lu, G. and Baowei, F., "Medical hyperspectral imaging: a review," J. Biomed. Opt. 19(1), 010901 (2014).
26. Grusche, Sascha, "Acquisition Techniques", Wikimedia Commons, 8 June 2014
27. Sellar, R. G. and Boreman, G. D., "Classification of imaging spectrometers for remote sensing applications," Opt. Eng. 44(1), 013602 (2005).
28. L. J. Hornbeck, "Digital Light ProcessingTM for High Brightness, High Resolution Applications," Proc. SPIE vol. 3013 (Electronic Imaging EI'97, Feb. 10-12, 1997, San Jose, CA)
29. Filipe Magalhães ; Mehrdad Abolbashari ; Francisco M. Araújo ; Miguel V. Correia and Faramarz Farahi "High-resolution hyperspectral single-pixel imaging system based on compressive sensing", Opt. Eng. 51(7), 071406 (2012).
30. Yitzhak August, Chaim Vachman, Yair Rivenson, and Adrian Stern, "Compressive hyperspectral imaging by random separable projections in both the spatial and the spectral domains," Appl. Opt. 52, D46-D54 (2013)
31. Xing Lin, Gordon Wetzstein, Yebin Liu, and Qionghai Dai, "Dual-coded compressive hyperspectral imaging," Opt. Lett. 39, 2044-2047 (2014)
32. M. E. Gehm, R. John, D. J. Brady, R. M. Willett, and T. J. Schulz, "Single-shot compressive spectral imaging with a dual-disperser architecture," Opt. Express 15, 14013-14027 (2007)

33. Michael A. Golub, Amir Averbuch, Menachem Nathan, Valery A. Zheludev, Jonathan Hauser, Shay Gurevitch, Roman Malinsky, and Asaf Kagan, "Compressed sensing snapshot spectral imaging by a regular digital camera with an added optical diffuser," Appl. Opt. 55, 432-443 (2016)

34. Gonzalo R. Arce, David J. Brady, Lawrence Carin, Henry Arguello and David S. Kittle, "Compressive coded aperture spectral imaging: An introduction", Signal Processing Magazine IEEE, vol. 31, no. 1, pp. 105-115, 2014.

35. August, Isaac et al. "Miniature Compressive Ultra-Spectral Imaging System Utilizing a Single Liquid Crystal Phase Retarder." Scientific Reports 6 (2016): 23524. PMC. Web. 2 Nov. 2017.

36. BECKER S, BOBIN J, CANDES E J, "NESTA: A Fast and Accurate First-order Method for Sparse Recovery", technical report, April 2009, California Institute of Technology

37. D.L. Donoho, "Compressed sensing," IEEE Trans. Inform. Theory, vol. 52, pp. 1289–1306, Sept. 2006.

38. E.J. Candès and T. Tao, "Near optimal signal recovery from random projections: Universal encoding strategies?," IEEE Trans. Inform. Theory, vol. 52, pp. 5406–5425, Dec. 2006.

39. E.J. Candès, "Compressive sampling," in Proc. Int. Cong. Mathematicians, Madrid, Spain, vol. 3, 2006, pp. 1433–1452.

40. David J. Starling, Ian Storer, and Gregory A. Howland, "Compressive sensing spectroscopy with a single pixel camera," Appl. Opt. 55, 5198-5202 (2016)

41. Abolbashari, M., MagalhÃĢes, F., AraÃējo, F. M. M., Correia, M. V., & Farahi, F. (2012). High dynamic range compressive imaging: a programmable imaging system. Optical Engineering, 51(7), 071407-1.
42. Kruse, F. A., A. B. Lefkoff, J. B. Boardman, K. B. Heidebrecht, A. T. Shapiro, P. J. Barloon, and A. F. H. Goetz, "The Spectral Image Processing System (SIPS) - Interactive Visualization and Analysis of Imaging spectrometer Data."Remote Sensing of Environment, 44:145 – 163 (1993).
43. Bland, J. Martin, and Douglas G Altman. "Statistical methods for assessing agreement between two methods of clinical measurement." The lancet 327.8476 (1986): 307-310.
44. G. Satat, M. Tancik and R. Raskar, "Lensless Imaging with Compressive Ultrafast Sensing", IEEE Trans. Computational Imaging vol. 3, 398-407 (2017)
45. Siegel, R. L., Miller, K. D. and Jemal, A. (2017), Cancer statistics, 2017. CA: A Cancer Journal for Clinicians, 67: 7–30. doi:10.3322/caac.21387
46. Surveillance, Epidemiology, and End Results (SEER) Program Populations (1969-2015) (www.seer.cancer.gov/popdata), National Cancer Institute, DCCPS, Surveillance Research Program, released December 2016.
47. Gage, I., Schnitt, S. J., Nixon, A. J., Silver, B., Recht, A., Troyan, S. L., ... & Connolly, J. L. (1996). Pathologic margin involvement and the risk of recurrence in patients treated with breast-conserving therapy. Cancer, 78(9), 1921-1928.
48. Bradley RS, Thorniley MS. A review of attenuation correction techniques for tissue fluorescence. Journal of the Royal Society Interface. 2006;3(6):1-13. doi:10.1098/rsif.2005.0066.

49. R. R. Anderson , “Polarized light examination and photography of the skin,” Arch. Dermatol. 127, 1000–1005 (1991)

50. Steven L. Jacques, Jessica C. Ramella-Roman, Kenneth Lee, "Imaging skin pathology with polarized light," J. Biomed. Opt. 7(3) (1 July 2002)

51. S. L. Jacques , R. J. Roman , and K. Lee , “Imaging superficial tissues with polarized light,” Lasers Surg. Med. 26, 119–129 (2000).

52. JC Ramella-Roman, K Lee, SA Prahl, SL Jacques ,“Design, testing, and clinical studies of a handheld polarized light camera”, Journal of Biomedical Optics, 2004

53. Tannous, Zeina & Y. Al-Arashi, Munir & Shah, Sonali & Yaroslavsky, Anna. (2009). Delineating Melanoma Using Multimodal Polarized Light Imaging. Lasers in surgery and medicine. 41. 10-6. 10.1002/

54. Vasefi F, MacKinnon N, Saager RB, et al. Polarization-Sensitive Hyperspectral Imaging in vivo: A Multimode Dermoscope for Skin Analysis. Scientific Reports. 2014;4:4924. doi:10.1038/srep04924.

Appendix: Publications

Joseph A. Peller, Kyle J. Thompson, Imran Siddiqui, John Martinie, David A. Iannitti, Susan R. Trammell, "Hyperspectral imaging based on compressive sensing to determine cancer margins in human pancreatic tissue ex vivo", Proceedings of SPIE Vol. 10060, 100600J (2017) SPIE Digital Library

Christopher R. Wilson, Joseph A. Peller, Susan R. Trammell, Pierce B. Irby, Nathaniel M. Fried, "Novel ureteroscope illumination designs", Proceedings of SPIE Vol. 10038, 100380P (2017) SPIE Digital Library

Joseph A. Peller, Faramarz Farahi, Susan R. Trammell, "Single-pixel hyperspectral imaging for real-time cancer detection: detecting damage in ex vivo porcine tissue samples", Proceedings of SPIE Vol. 9791, 97910O (2016) SPIE Digital Library

Joseph A. Peller, A. E. Shipley, Susan R. Trammell, Mehrdad Abolbashari, Faramarz Farahi, "A novel spectral imaging system for use during pancreatic cancer surgery", Proceedings of SPIE Vol. 9420, 94200Q (2015) SPIE Digital Library